Loss of *Nmp4* optimizes osteogenic metabolism and secretion to enhance bone quality

Yu Shao[1], Emily Wichern[2], Paul J. Childress[3, 4], Michele Adaway[2], Jagannath Misra[5], Angela Klunk[2], David B. Burr[2, 4, 6], Ronald C. Wek[5], Amber L. Mosley[5], Yunlong Liu[1], Alexander G. Robling[2, 4], Nickolay Brustovetsky[7], James Hamilton[7], Kylie Jacobs[8], Deepak Vashishth[9], Keith R. Stayrook[10], Matthew R. Allen[2, 4, 11], Joseph M. Wallace[3, 4, 6, ¶] Joseph P Bidwell[1, 2, 4¶]

1. Department of Medical and Molecular Genetics, Indiana University School of Medicine (IUSM), Indianapolis, IN, 46202
2. Department of Anatomy & Cell Biology, Indiana University School of Medicine (IUSM)
3. Department of Orthopaedic Surgery, IUSM
4. Indiana Center for Musculoskeletal Health
5. Department of Biochemistry & Molecular Biology, IUSM
6. Department of Biomedical Engineering, Indiana University-Purdue University at Indianapolis, IN, 46202
7. Department of Pharmacology & Toxicology, IUSM
8. Department of Microbiology & Immunology, IUSM
9. Center for Biotechnology & Interdisciplinary Studies (Rm 2213) and Department of Biomedical Engineering, Rensselaer Polytechnic Institute, 110 8th Street, Troy, NY 12180, USA
10. Lilly Research Laboratories, Eli Lilly and Company, Indianapolis, Indiana 46202
11. Roudebush Veterans Administration Medical Center, Indianapolis, IN

Running title: Nmp4 regulates bone matrix secretion

Key terms: Metabolism, osteoporosis, parathyroid hormone, raloxifene, Seahorse Assay, transcriptome, ultimate stress, yield stress

---

This is the author's manuscript of the article published in final edited form as:
Shao, Y., Wichern, E., Childress, P. J., Adaway, M., Misra, J., Klunk, A., … Bidwell, J. P. (2019). Loss of Nmp4 optimizes osteogenic metabolism and secretion to enhance bone quality. American Journal of Physiology-Endocrinology and Metabolism. https://doi.org/10.1152/ajpendo.00343.2018

¶Corresponding Authors:

Joseph P. Bidwell

Department of Anatomy & Cell Biology

Indiana University School of Medicine

Medical Science Bldg 5035, 635 Barnhill Drive

Indianapolis, IN 46202

E-mail: jbidwell@iupui.edu

Joseph M. Wallace

Department of Biomedical Engineering

Indiana University-Purdue University at Indianapolis

SL 220

Indianapolis, IN 46202

E-mail: jmwalla@iupui.edu

Yu Shao and Emily Wichern contributed equally to this study.

Disclosure statement: Y.S, E.W., P.J.C., M.A., J.M, A.K., D.B.B., R.C.W., A.L.M., Y.L., A.G.R, N.B., J.H., K.J., D.V., M.R.A., J.M.W, and J.P.B. have nothing to disclose. K.R.S. is an employee of Eli Lilly and Company

ABSTRACT:

A goal of osteoporosis therapy is to restore lost bone with structurally sound tissue. Mice lacking the transcription factor Nuclear Matrix Protein 4 (*Nmp4, Zfp384, Ciz, ZNF384*) respond to several classes of osteoporosis drugs with enhanced bone formation compared to wild type (WT) animals. *Nmp4*$^{-/-}$ mesenchymal stem/progenitor cells (MSPCs) exhibit an accelerated and enhanced mineralization during osteoblast differentiation. To address the mechanisms underlying this hyper-anabolic phenotype, we carried out RNA-sequencing and molecular and cellular analyses of WT and *Nmp4*$^{-/-}$ MSPCs during osteogenesis to define pathways and mechanisms associated with elevated matrix production. We determined that *Nmp4* has a broad impact on the transcriptome during osteogenic differentiation, contributing to the expression of over 5,000 genes. Phenotypic anchoring of transcriptional data was performed for the hypothesis-testing arm through analysis of cell metabolism, protein synthesis and secretion, and bone material properties. Mechanistic studies confirmed that *Nmp4*$^{-/-}$ MSPCs exhibited an enhanced capacity for glycolytic conversion- a key step in bone anabolism. *Nmp4*$^{-/-}$ cells showed elevated collagen translation and secretion. Expression of matrix genes that contribute to bone material-level mechanical properties were elevated in *Nmp4*$^{-/-}$ cells, an observation that was supported by biomechanical testing of bone samples from *Nmp4*$^{-/-}$ and WT mice. We conclude that loss of *Nmp4* increases the magnitude of glycolysis upon the metabolic switch, which fuels the conversion of the osteoblast into a super-secretor of matrix resulting in more bone with improvements in intrinsic quality.

INTRODUCTION:

Osteoporosis is a disease of attenuated bone mass and strength that significantly increases the risk of fragility fractures (92). Teriparatide (PTH) and abaloparatide (PTHrP) are currently the only FDA-approved osteoanabolic therapies for this disease (52, 61). These drugs add new bone to the osteoporotic skeleton whereas the primary effect of anti-catabolic drugs is a reduction in the pathologically elevated bone resorption (30). The benefits of PTH treatment include an increase in bone mass through a combination of new bone modeling and the sustained bone remodeling with a positive balance as well as improved bone material properties (13, 18, 29, 32, 59). However, the potency of PTH precipitously declines and there is an FDA-mandated two-year limit on treatment (18), emphasizing the need for new strategies that improve the efficacy of the drug, such as by combining hormone treatment with an anti-catabolic drug or targeting PTH directly to bone (26, 83). Neutralizing intrinsic pathways that temper PTH-induced osteoblast secretion of bone matrix might improve drug efficacy. Indeed, a similar strategy of “inhibiting the inhibitor” (46) has led to the development of the osteoanabolic romosozumab, a monoclonal antibody that neutralizes the action of the osteoinhibitory protein sclerostin, currently under consideration by the FDA for clinical approval (3, 94).

We reported that the transcription factor Nuclear Matrix Protein 4 (*Nmp4, Zfp384, Ciz, ZNF384*) suppresses the action of osteoanabolics (15, 16, 41, 70, 90, 95) and thus elucidation of the upstream and downstream effectors in the Nmp4 pathway may provide a map of the innate barriers to PTH-induced bone formation. Indeed, as a trans-acting protein Nmp4 is well positioned to control multiple aspects of bone formation. Genome-wide Chromatin Immunoprecipitation followed by high-throughput sequencing (ChIP-seq) analysis in MC3T3-E1 cells suggested that Nmp4 has wide ranging effects on the transcriptome, with over 15,000 Nmp4 binding sites in the osteoblast genome. Of importance, nearly 70% of these sites are within -5 and +2 kb from a transcription start site (TSS) or within introns, both DNA regions that often harbor regulatory regions (16).

Nmp4$^{-/-}$ mice exhibit more bone marrow osteoprogenitors than their WT littermates (16, 41, 95). Expanded cultures of *Nmp4*$^{-/-}$ mesenchymal stem/progenitor cells (MSPCs) induced with osteogenic medium exhibit elevated mRNA expression of the bone matrix proteins type I collagen (*Col1a1*), osteocalcin (*Bglap2*), and osteopontin (*Spp1*). Additionally, the anabolic process of ribosome biogenesis is elevated in these cells, as is the expression of *Gadd34* (*PPP1r15a*), which helps maintain translation and ultimately contributes to the continued trafficking of secretory protein through the endoplasmic reticulum (ER) despite increased protein loads (16, 20, 114).

To address the cellular pathways by which Nmp4 suppresses osteoblast-mediated bone formation we performed high-throughput RNA sequencing (RNA-seq) of WT and *Nmp4*$^{-/-}$ expanded MSPCs during osteogenesis. Network analyses of the RNA-seq output were used for driving hypothesis testing, i.e. select pathways that were significantly altered in the transcriptome were evaluated experimentally. The results phenotypically anchored bioinformatic predictions to changes in metabolic and biochemical properties of the *Nmp4*$^{-/-}$ osteogenic cells. Based on the RNA-seq data we hypothesized that *Nmp4*$^{-/-}$ osteoblasts elaborate a matrix that improves bone material and structural characteristics. Therefore we examined these bone properties from experimental WT and *Nmp4*$^{-/-}$ mice that had undergone various osteoporosis therapies. These data reveal new aspects of how loss of *Nmp4* alters bone matrix secretion as well as the impact of this single gene on bone quality.

MATERIALS AND METHODS

Cell culture: MSPCs were derived from individual mice as previously described (16, 109). Briefly, long bone marrow (BM) was harvested from euthanized mice 6–8 weeks of age, and a Ficoll gradient was used to isolate the mononuclear cells. These cells were seeded in Mesencult Media^{TM} + Mesencult Stimulatory Supplement^{TM} (StemCell Technologies, Vancouver Canada) and sustained for 3–4 weeks without passage while fed every 5–7 days by removing 50% of the

old media and adding 50% fresh media, so as not to disturb the cells. Upon reaching 80% confluence, the cells were passaged at 1:3 dilution for 2 additional passages before use in experiments or were frozen for stock vials. Cells were used for study between passages 5–10. To assess the mineralization phenotype of each MSPC preparation, cells were seeded in α-MEM supplemented with 100 IU/mL penicillin, 100 µg/mL streptomycin, 25 µg/mL amphotericin, 2 mM L-glutamine (Gibco BRL, Life technologies; Grand Island, NY, USA) and 10% fetal bovine serum (Sigma-Aldrich, St. Louis, MO). At 48 hours post-seeding the medium was refreshed and further supplemented with ascorbic acid (5 µg/mL; Sigma-Aldrich), dexamethasone (10 nM; Sigma-Aldrich), and 10 mM glycerol 2-phosphate disodium salt hydrate (BGP) (Sigma-Aldrich). To visualize the mineralization in culture, cells were stained with alizarin red as previously described (16).

RNA-seq analysis: To compare transcriptome profiles of non-differentiating and osteogenic-differentiating WT and *Nmp4*$^{-/-}$ MSPCs, cells were seeded into 12-well plates at either 10,000 cells/well (25 cells/mm^2) or 25,000 cells/well (62 cells/mm^2). The cells seeded at the lower density were maintained in Mesencult Media^{TM} + Mesencult Stimulatory Supplement^{TM} (non-differentiating medium) for 3 days post-seeding and then harvested for total RNA. Cells plated at the higher density were maintained in α-MEM complete medium throughout the experiment. At 48 hours post-seeding the medium was refreshed with the ascorbic acid, dexamethasone, and BGP supplement. These cells were harvested at 7 days post-seeding as early osteogenic cells.

Total RNA was harvested using RNeasy (Qiagen, Valencia, CA) and measured for quality using the Agilent 2100 Bioanalyzer, and Qubit 2.0 Fluorometer. High RNA integrity is critical for evaluating the transcriptome. The RNA integrity number (RIN) is an algorithm for assigning integrity values to RNA measurements and assigns an electropherogram a value of 1 to 10, with 10 being the least degraded. All RIN numbers for our samples ranged between 8.2-

9.7. A conservative cut-off value in the context of RNA degradation lies between 6.4 and 7.9 (31), well below our values. Four technical replicates were harvested for each time point and genotype. Total RNA samples were submitted to the Beijing Genomics Institute (BGI) for transcriptome sequencing. In brief, magnetic beads with Oligo (dT) were used to isolate mRNA. The mRNA was fragmented and then constructed into HiSeq 2000 strand-specific libraries. The 2 × 100-nt paired-end reads were generated by Illumina HiSeq^{TM} 2000. Clean reads filtered from raw sequence reads were returned from BGI. Raw reads were filtered into clean reads by employing the following rules: (i) remove reads in which the percentage of bases with quality <10 was >50%; (ii) remove reads in which unknown bases were more than 10%; (iii) remove reads with adapters; (iv) map the clean reads to Mus musculus reference mm10 using STAR (version 2.4.2a) (23); (v) gene-based expression levels were quantified with featureCounts (58); (vi) differential expression of genes across different treatments was determined with edgeR (88) [GEO accession number GSE112694]

RNA-seq determines the relative amount of each gene in each RNA sample but does not provide any measure of the total RNA output on a per-cell basis. This can be important when some genes are very highly expressed in one sample but not another (89), which is the case for our *Nmp4*$^{-/-}$ phenotype. We have previously shown that the *Nmp4*$^{-/-}$ MSPCs express upwards to 2-fold more RNA/cell than WT cells (114). Therefore we used GusB as a scaling factor for the present RNA-seq data since our previous work identified GusB as an appropriate normalizer for microarray data (16).

Pathway enrichment analysis was performed using the Ingenuity Pathway Analysis software (IPA, Ingenuity Systems, Inc., Redwood City, CA, USA) to distinguish significant canonical pathways in which the Differentially Expressed Genes (DEGs) identified in the WT and *Nmp4*$^{-/-}$ samples were enriched. Fisher's exact test was used to compute a p-value that denotes the probability of the DEGs in the pathway being found together due to random chance.

We also applied the Benjamini-Hochberg false discovery rate (FDR) ($q < 0.05$) correction to account for multiple comparisons in the IPA.

We define a candidate Nmp4 direct target gene as a gene whose expression is altered with the loss of *Nmp4* and also supports Nmp4 occupancy. To identify candidate genes we performed Venn diagram analysis with the gene lists from the present RNA-seq dataset and lists derived from our previous study of the Nmp4 genome-wide occupancy by ChIP-Seq in MC3T3-E1 preosteoblasts (16). This cell line is an established *in vitro* model for osteoblastogenesis. Genes that were identified as supporting Nmp4 occupancy exhibited ChIP-seq peaks within -5 to +2 kb from a transcription start site (TSS) and/or within the range defined by the TSS and the transcription end site, and not within the promoter range of the same gene (Table S1 https://figshare.com/s/aef3382cdc7c02151e6f**,** GEO accession number GSE112693 for complete ChIP-Seq dataset) (16). Additionally, we further refined this definition by using only genes contained in both the ChIP-seq and RNA-seq lists.

Seahorse assay: Four independent MSPC cell preparations were used in the metabolic stress tests. The MSPCs $1957R^{WT}$ and $1957N^{KO}$ were derived from male littermates obtained from an $Nmp4^{+/-}$ x $Nmp4^{+/-}$ cross. The $1584L^{WT}$ and $1515RR^{KO}$ MSPCs were derived from mice obtained from different litters and different parents. Cells were seeded into an XFe24 well plate and grown for ~24hrs in culture. MSPCs were then subjected to mitochondrial stress tests using oligomycin, carbonyl cyanide-4 (trifluoromethoxy) phenylhydrazone (FCCP), rotenone, and antimycin A per the manufacturer's instructions (Seahorse Biosciences, Lexington, MA). Glycolysis stress tests were performed using oligomycin and 2-deoxy-D-glucose (Seahorse Biosciences). After each analysis, total cell number was quantified and normalized to O_2 consumption rate (OCR) or extracellular acidification rate (ECAR), respectively. Glycolytic and mitochondrial stress tests were repeated 4-5 times each (biological replicates). We pooled all

data (each well) obtained from the glycolytic or mitochondrial tests as technical replicates for statistical analysis.

Collagen secretion analysis: All six independent MSPC cell preparations were used in the collagen secretion assays including $1957R^{WT}$, $1584L^{WT}$, $2001RL^{WT}$, $1957N^{KO}$, $1515RR^{KO}$, and $1986R^{KO}$. Collagen levels were determined using the Sircol assay (Biocolor Ltd, Carrickfergus, Northern Ireland) (1, 62). Non-differentiating WT and *Nmp4*$^{-/-}$ MSPCs, cells were seeded into 12-well plates at 10,000-20,000 cells/well (25-50 cells/mm^2). These cells were maintained in Mesencult Media^{TM} + Mesencult Stimulatory Supplement^{TM} (non-differentiating medium) for 4 days post-seeding. To harvest the acid soluble fraction, cultures were washed twice with ice-cold PBS and then scraped into PBS containing 0.5M acetic acid and digested overnight at 4-8°C. The samples were then snap frozen. Collagen was concentrated from these acid-soluble fractions and then analyzed according to the manufacturer's instructions. The collagen amount was normalized to cell number or presented as collagen/well vs. cell number/well. All experiments were repeated at least twice. All the data shown in the assays are an average of at least 4-5 different wells per group.

Col1a1 polysome analysis: Preparations from four independent MSPC cell preparations, designated $1957R^{WT}$, $1957N^{KO}$, $1584L^{WT}$, and $1515RR^{KO}$, were used to measure collagen mRNA in polysomes. Equal amounts of WT and *Nmp4*$^{-/-}$ MSPCs were cultured into 10cm culture plates and maintained in Mesencult Media^{TM} + Mesencult Stimulatory Supplement^{TM} for 4 days. On Day 4, cycloheximide was added to each culture dish for 10min prior to harvesting. Cells were rinsed with ice-cold phosphate-buffered saline (PBS) solution containing 50 µg/ml cycloheximide and then lysed with 500µl of cold lysis buffer containing 10mM Tris-HCl (pH 7.4), 300mM KCl, 10mM $MgCl_2$, 1mM DTT and 50µg/ml cycloheximide, followed by centrifugation at 13000 rpm for 10min at 4°C. Cell lysates were then applied to the top of 10-50% sucrose

gradients and subjected to ultracentrifugation in a Beckman SW41Ti rotor at 40,000 rpm for 2 h at 4°C. Using a piston gradient fractionator, polysome profiles of each sample was recorded at 254 nM by a UV monitor with Data Quest software as described previously (103). TRIzol LS reagent (Life Technologies, Inc) was used to purify RNA present in each of the sucrose gradient fractions. To insure that there was uniform RNA preparation between fractions, equal amount of firefly luciferase mRNA was added to each fraction. RNA prepared from equal volumes of each fraction was then used as a template for cDNA synthesis utilizing the TaqMan RT kit (Life Technologies, Inc.). The qPCR analyses of firefly luciferase and *Col1a1* transcripts were measured as described previously (2). Equal amounts of firefly luciferase mRNA was measured in each of the fractions. Primer sequences for both transcripts were *Col1a1* F: 5'-ACGTCCTGGTGAAGTTGGTC-3', R: 5'-CAGGGAAGCCTCTTTCTCCT-3'; *firefly luciferase* F: 5'-CCAGGGATTTCAGTCGATGT-3', R: 5'-AATCTCACGCAGGCAGTTCT-3'. Experiments were carried out two independent times with similar results.

Mice: WT and *Nmp4*$^{-/-}$ mice were generated as previously described and maintained at Indiana University Bioresearch Facility School of Dentistry (90). Briefly the strategy for preparing the global *Nmp4*$^{-/-}$ mice involved removing the region of this gene containing coding exons 4 – 7 via homologous recombination (90). The correctly targeted embryonic stem (ES) cell lines from 129SvEv ES clones were microinjected into C57BL/6J blastocysts and the chimeric mice were crossbred with the C57BL/6J mice (The Jackson Laboratory, Bar Harbor, ME) to generate germline transmission. These mice were backcrossed for seven generations on the C57BL/6J background. Their WT littermates were used as the control mice for these experiments. The mice were housed, 2-4 mice/cage, under a 12hr light/12 hour dark regimen and Labdiet Rodent 5001 diet was provided ad libitum. The Indiana University Institutional Animal Care and Use Committee approved all experimental procedures described in the present study.

Therapies: At 10 weeks of age virgin female mice were randomly sorted into eight treatment groups by weight and genotype. Each mouse received two sequential 100µl injections/day containing the drugs or vehicle(s) 7 days/week for 7 weeks. Mice in select groups were injected subcutaneously with synthetic human PTH (hPTH) 1–34 acetate salt (Bachem Americas, Inc. Torrance, CA) at 30 µg/kg/d, daily, a dose often used in rodents to evaluate PTH bone anabolic action in vivo (37, 63). The dose of the anti-catabolic agent raloxifene (RAL, Sigma-Aldrich) is based on human clinical doses. RAL is normally administered as a 60mg daily dose, therefore based on a 60kg patient the quantity would be 1 mg/kg/day. The assumption is 100% absorption therefore the full dose was administered as a subcutaneous injection (95). Our euthanasia protocol involves using carbon dioxide inhalation at 20%V/min followed by bilateral pneumothorax or cervical dislocation in compliance with the guidelines of our Animal Care and Use Committee. This is an approved method by the Panel on Euthanasia of the American Veterinary Medical Association.

Micro-computed tomography (µCT): Femurs and L5 vertebra were dissected from the 17 week-old mice. The femurs were soaked in 0.9% saline, wrapped with gauze and stored at –20°C. The L5 vertebra were transferred to 10% formalin for 2 days and then stored in 70% ethanol. Left femurs were thawed to room temperature and scanned while hydrated with a 8.5 µm voxel size using a Skyscan 1172 µCT system (176 mA, 0.5 mm Aluminum filter). Scans were reconstructed with voxel attenuation coefficients ranging from 0-0.11, a beam hardening correction of 40%, and a ring artifact correction of 5. Mineral density was calculated using daily scans of manufacturer supplied hydroxyapatite (HA) phantoms of 0.25 g/cm^3 and 0.75 g/cm^3. L5 vertebrae were scanned with a 6 µm voxel size using the Skyscan 1172 µCT system (176 mA, 0.5 mm Aluminum filter). Scans were reconstructed with voxel attenuation coefficients ranging from 0-0.08, a beam hardening correction of 20%, and a ring artifact correction of 10. Three-dimensional reconstructions using Skyscan software provided femur and L5 vertebra trabecular

bone volume per total volume (BV/TV, %). Parameters obtained for femoral cortical bone included total cross-sectional area (CSA, mm^2), marrow area (mm^2), cortical thickness (mm), periosteal bone surface (BS, mm), endocortical BS (mm), anterior-posterior width (AP, mm), medial-lateral width (ML, mm), AP/ML, moment of inertia about the AP axis ($I_{ap,}$ mm^4), moment of inertia about the ML axis (I_{ml}, mm^4), maximum moment of inertia (I_{max}, mm^4), minimum moment of inertia (I_{min}, mm^4), medial extreme (mm), and tissue mineral density (TMD, g/cm^3 HA).

Mechanical testing: Left femurs from each animal were thawed to room temperature and monotonically tested to failure in three-point bending at a displacement rate of 0.025 mm/sec using a support span of 9 mm (4). The bones were oriented in the anterior-posterior direction with the anterior side in tension. The moment of inertia about the medial-lateral axis and the extreme fiber in the anterior direction were obtained from the μCT images using a seven slice region centered on the failure site, and were utilized to map load-displacement to stress-strain, employing standard beam bending equations. Structural-level mechanical and tissue-level material properties were then obtained from the load-displacement and stress-strain curves.

Statistical analysis: We used the statistical package JMP version 7.0.1 (SAS Institute, Cary, NC) to evaluate osteoporosis treatment response in our experimental mice. We tested three experimental therapies and a vehicle control using two genotypes of mice, yielding a total of eight treatment groups. Outliers in the datasets were identified using the interquartile range (IQR) method to assess statistical dispersion (68). The remaining data were analyzed with a 2-way ANOVA for effects of genotype and treatment followed by a Tukey-Kramer post hoc test for comparison of more than two groups or Student t post hoc test for comparing WT and *Nmp4*$^{-/-}$ parameters as two groups. Experimental data were sorted by either treatment or genotype to determine whether either or both influenced the value of the endpoint parameter and whether genotype affected the response to treatment (genotype x treatment interaction). To assess if the

combination treatment provided a synergistic effect over the mono-therapies we performed 2-way ANOVA tests using PTH and RAL as the independent variables on both WT and *Nmp4*$^{-/-}$ datasets. Statistical significance was set at $p \leq 0.05$. To evaluate the metabolic profiles of the MSPCs, we used the Statistical Analysis System version 9.4 (SAS Institute) and JMP to perform student t-tests in comparing specific metabolic parameters. Finally, ggplot2 was used to create all the heatmaps, volcano plots, and boxplots (107).

RESULTS:

Nmp4 regulates a large portion of the osteogenic transcriptome

We previously showed that expanded cultures of *Nmp4*$^{-/-}$ bone marrow MSPCs exhibited a precocious and enhanced mineralization compared to WT cells (16). For the present study, three independently derived WT MPSCs from individual isogenic mice, along with three *Nmp4*$^{-/-}$ preparations confirmed that the *null* cells exhibited mineralization typically within 1 week of exposure to osteogenic medium compared to 2-3 weeks for the WT cells (Figure 1A).

To address the mechanism for the hyper-anabolic phenotype elicited by loss of *Nmp4*, we performed transcriptome analysis on osteogenic MSPCs as a guide for hypothesis testing. Given that there were some variations in time to mineralization between the individual *Nmp4*$^{+/+}$ and *Nmp4*$^{-/-}$ MSPC preparations, we elected to carry out RNA-seq on the MSPCs 1584L^{WT} vs. 1515RR$^{Nmp4-/-}$ under two distinct culture conditions. These cells exhibited a striking difference in the time to mineralization onset. We then carried out the critical phenotypic anchoring experiments with the other MSPC preparations as well as the WT and *Nmp4*$^{-/-}$ mice to show that our findings are broadly applicable.

To perform RNA-seq analysis, RNA was harvested from cells at Day 3 post-seeding that were maintained in non-differentiation medium and at Day 7 in culture in which the cells had been transferred to osteogenic medium 48hrs post-seeding. All data obtained from these studies including the differences observed in mRNA expression between the WT and *Nmp4*$^{-/-}$

MPSCs at different time points following exposure to osteogenic medium are provided in Table S2 https://figshare.com/s/aef3382cdc7c02151e6f. A volcano plot shows that *Nmp4*-deleted cells cultured in non-differentiating medium for 3 days displayed significant ≥ 2-fold change in the expression of 5032 genes compared to WT. Of these, there was an increase in the expression of 3468 genes and a decrease in expression of 1564 genes (Figure 1B). Following this criterion, the expression profiles of 8438 genes were not significantly affected by *Nmp4* status (Figure 1B).

Loss of *Nmp4* had a similar impact on the transcriptome of MSPCs maintained in the osteogenic differentiating medium and harvested at Day 7, which coincided with the initiation of mineralization. At the 7-day time point, the expression profiles of 5313 genes were significantly altered by ≥ 2-fold, with 3925 genes presenting an elevation in expression compared to WT cells and 1388 genes showing a decrease (Figure 1B). *Nmp4* status did not impact the expression of 8151 genes in cells maintained in the osteogenic medium (Figure 1B).

We recently reported a genome-wide ChIP-seq analysis of Nmp4 binding in MC3T3-E1 pre-osteoblasts that identified over 15,000 binding sites for this transcription factor (16). This cell line is an established *in vitro* model for early osteoblastogenesis that is similar to our primary MSPCs. To identify genes that are direct targets of Nmp4, we determined the overlap of the gene lists derived from the present MSPC RNA-seq datasets and those lists derived from our previous analysis of Nmp4 genome-wide ChIP-Seq analysis (16). The gene list used from the ChIP-seq dataset contained genes that had 1 or more peaks associated with the transcription start site (TSS) within -5 to +2 kb from a TSS and/or within the range defined by the TSS and the transcription end site (TES), and not within the promoter range of the same gene (Table S1) (16). Additionally, we limited the compilation to 4786 and 4787 genes expressed by our MSPCs for days 3 and 7 in culture respectively. The Venn diagrams revealed that about 28% of the genes occupied by Nmp4 exhibited a significant increase in expression upon loss of this

transcription factor after 3 and 7 days in culture, indicating gene repression by Nmp4. By contrast, ~9% showed a decrease in expression upon loss of *Nmp4* suggesting that Nmp4 functions to directly activate these gene targets (Figures 1D & 1E). Expression of ~63% of the genes that supported Nmp4 with significant occupancy were not strongly impacted by loss of *Nmp4*, suggesting that Nmp4 status alone is not sufficient to alter the expression of these genes (Figures 1D & 1E). We conclude that in this osteogenic context Nmp4 has an extensive influence on the MSPC and osteogenic transcriptomes consistent with its widespread occupancy in their genomic landscapes.

Loss of Nmp4 alters pathways that exhibit the dual functions of driving osteogenesis and glycolysis

To identify cellular pathways sensitive to *Nmp4* status, we performed IPA (Ingenuity pathway analysis)-based network analyses on the 5032 genes that exhibited a significant change in expression between the *Nmp4*$^{-/-}$ and WT cells at Day 3 (non-differentiating medium) and on the 5313 genes that exhibited a change in expression at Day 7 (osteogenic medium) in culture. Tables S3 and S4 list the 252 significant canonical pathways derived from transcriptome analysis of Day 3 and the 201 significant canonical pathways derived from analysis of Day 7 cells, respectively https://figshare.com/s/aef3382cdc7c02151e6f. The large number of affected pathways is consistent with the substantial number of genes whose expression is influenced by *Nmp4* status.

Many of the canonical pathways listed in Tables S3 & S4 were also identified in previous studies characterizing MSC transcriptomic changes during osteogenic differentiation (11, 72, 80), thus supporting our experimental approach. For example, transforming growth factor-β (TGF-β) signaling, IGF1, Wnt/β-catenin signaling, and bone morphogenic protein (BMP) signaling all appear to support human adipose-derived stem cells (hASC) and bone marrow

stromal cell (BMSC) osteogenesis. Additionally, many pathways related to the triggering of cell cycle, growth, differentiation, and migration, such as axonal guidance signaling, platelet-derived growth factor signaling (PDGF signaling), integrin signaling, and actin cytoskeleton signaling, have previously been distinguished in these MSPC preparations (11, 72, 80) and were identified here.

In our hypothesis-generating screen of the IPA outcomes we identified several pathways predicted to be sensitive to *Nmp4* status and drive both osteogenesis and metabolic reprogramming necessary for fueling the development of the professional secretory osteoblast (Tables S3 and S4) (56, 79, 81, 96). Several pathways were common to cells harvested on either Day 3 or Day 7 and we present some of these data in graphical form for Day 7 (Figures 2A & 2B). The bar graphs in Figure 2A are color-coded to reflect the z-score calculated by the IPA algorithm, which predicts the direction of change for the pathway upon loss of *Nmp4*. An absolute z-score of 2 or more is considered significant. The activation state of the pathway is predicted to be increased if the z-score is ≥ 2 and these bars are color coded with an orange hue. Conversely, bar graphs with a blue hue indicate a z-score ≤ -2 representing canonical pathways with a decreased activity. Those pathways represented with a grey bar (z = NaN) indicate that the z-score algorithm cannot predict whether the pathway activity is increased or decreased in the *Nmp4*$^{-/-}$ cells.

The bar graphs in Figure 2B are color coded to reflect the percentage of genes in a particular pathway whose expressions are upregulated (red) or downregulated (green). For example, the Wnt/Ca^{+2} signaling pathway z scores were $+3.00^{Day3}$/$+3.77^{Day7}$, (Figure 2A; Tables S3 and S4) indicating that loss of *Nmp4* enhances the activity of this pathway. Additionally a high percentage of the genes in this pathway exhibited a significant increase in expression in the *Nmp4*$^{-/-}$ MSPCs (Figure 2B). This is significant to the *Nmp4*$^{-/-}$ osteoblast phenotype since Wnt signaling is a major driver of bone anabolism and advances osteogenesis in part through its stimulation of glycolysis (27). The IPA's Molecule Activity Predictor (MAP) algorithm allowed

simulating the effects of disabling *Nmp4* on the Wnt signaling pathway, which predicted elevated beta catenin activity, a key driver of osteogenesis (49), and the attenuated activity of Nemo-like kinase (NLK), a suppressor of beta-catenin transcriptional activity and osteogenesis (9, 44, 74) (Figure 3). The accompanying Wnt pathway heatmap (Figure 3) suggests this predicted increase in Wnt signaling activity is based, in part, on the diminished expression of numerous Wnt inhibitors including *Wif1*, *Sfrp1*, *Sfrp2*, and *Apc2* (7, 101).

Of interest, loss of *Nmp4* significantly enhanced the expression of *Dkk2* mRNA (see heatmap Figure 3). Depending on the cellular context *Dkk2* can stimulate or inhibit Wnt signaling (55, 64). For example, Dkk2 is essential for osteoblast terminal differentiation, mineralization and may be a novel mediator of the PTH-induced anabolic response in bone (57, 111). The activities of the Igf1 ($z = +4.13^{Day3}$) and the Nrf2 signaling pathways ($z = +4.33^{Day3}$; $+4.23^{Day7}$) were predicted to be upregulated in *Nmp4*$^{-/-}$ cells and although loss of *Nmp4* was projected to alter the Hif1α signaling pathway the direction of activity could not be ascertained ($z = NaN^{Day3}$; $z = NaN^{Day7}$) (Figure 2; Tables S3 and S4). Nevertheless all pathways regulate osteogenesis as well as govern cellular metabolic reprogramming (28, 39, 82, 85). Furthermore, the PTEN network was significantly sensitive to *Nmp4* status and assigned z scores -2.50^{Day3} and -1.76^{Day7} (Figure 2; Tables S3 and S4) suggesting that the activity of this pathway is attenuated with loss of *Nmp4*. Indeed, depletion of PTEN signaling was reported to enhance osteoprogenitor expansion and glycolytic conversion (35, 110).

Of interest, loss of *Nmp4* did not significantly alter the expression of *Runx2* and *Sp7* (*Osterix*), master regulators of osteogenesis, but elevated expression of the transcription factors *Tcf4*, *Atf4*, and *Ddit3* (*Chop, Gadd153*), which all function downstream of *Runx2* and *Sp7* (Figure 4). Additionally *Nmp4*$^{-/-}$ cells exhibited decreased mRNA expression of transcription factors that drive adipogenesis or chondrogenesis suggesting that loss of *Nmp4* facilitates MSPC differentiation towards osteogenesis and that this predisposition is reinforced by shifts in

transcriptional networks regulating the activities of the aforementioned osteogenic/metabolic pathways (Figure 2, Figure 4 Tables S3 and S4).

Phenotype anchoring of our transcriptional data confirmed Nmp4$^{-/-}$ MSPCs exhibited an enhanced capacity for glycolytic conversion

The glycolytic pathway is predicted to be altered in the *Nmp4*$^{-/-}$ cells at both Day 3 and Day 7 in culture (Figure 2; Tables S3 and S4). A heatmap of several genes that comprise the glycolytic pathway showed that loss of *Nmp4* greatly elevated the expression of the glucose transporter *Slc2a1* (a.k.a *Glut1*) and increased the transcript levels of both *Slc2a3* and *Slc2a4* (*Glut3*, *Glut4*, Figure 5A). The lactate transporter *Slc16a3* (a.k.a *Mct4*) was highly expressed in the *Nmp4*$^{-/-}$ MPSCs at both Day 3 and Day 7 in culture (Figure 5A). A primary function of *Slc16a3* is the secretion of lactate and protons from highly glycolytic cells (22) and a recent study determined that increased levels of Slc16a3 is necessary for sustaining high glycolysis in macrophages (102). Several genes mediating the conversion of glucose to pyruvate displayed significantly elevated expression in *Nmp4*$^{-/-}$ cells (Figure 5A). Genes responsible for regulating the switch between aerobic glycolysis and oxidative phosphorylation including *Hk2*, *Pkm*, *Pdk1*, and *Ldha* showed significantly higher mRNA levels in the *Nmp4*$^{-/-}$ cells. Additionally, our ChIP-seq analysis in MC3T3-E1 cells showed that Nmp4 binds to both *Pdk1* and *Pkm* genes (Figure 5B) indicating that this trans-acting protein directly targets key genes that regulate the glycolytic switch.

We linked our transcriptome/ChIP-seq analyses to functional data via the glycolytic stress tests (Figure 6). WT vs. *Nmp4*$^{-/-}$ cells derived from the male littermates (1957^{WT}/1957^{KO}) and the WT vs. *Nmp4*$^{-/-}$ cells derived from the males obtained from random litters (1584L^{WT}/1515RR^{KO}) were cultured in non-differentiating medium using the Seahorse analyzer. Cells were seeded directly into an analyzer well plate and grown for 24hrs in culture. Subsequently cells were incubated in medium devoid of glucose or pyruvate and the analyzer

452 measured the extracellular acidification rate (ECAR) before and after a saturating amount of
453 glucose was injected. These experiments quantified glycolytic activity (glycolysis), which was
454 significantly elevated in *Nmp4*$^{-/-}$ cells (Figures 6A-6C). The ECAR value was then obtained after
455 injection of oligomycin, which inhibited oxidative phosphorylation driving the cell to use
456 glycolysis to its maximum capacity (glycolytic capacity). Again the *Nmp4*$^{-/-}$ cells exhibited a
457 significantly elevated level for this parameter (Figures 6A-6C). The final injection of 2-deoxy-
458 glucose (2-DG), a glucose analog that inhibited glycolysis through competitive binding to
459 glucose hexokinase, decreased ECAR confirming that the lowered medium pH was the result of
460 increased glycolysis (Figures 6A and 6B). The glycolytic reserve, defined as the difference
461 between glycolytic capacity and glycolysis rate was elevated with the loss of *Nmp4* (Figures 6A-
462 6C). We conclude that loss of *Nmp4* results in the metabolic reprogramming of the MSPCs
463 enhancing their capacity for glycolysis.
464
465 *Nmp4*$^{-/-}$ *MSPCs exhibited an increased mitochondrial respiratory capacity*
466 Next the mitochondrial respiratory capacity was compared in the WT and *Nmp4*$^{-/-}$ cells.
467 For the mitochondrial stress test the Seahorse analyzer was used to measure basal respiration
468 reported as oxygen consumption rate (OCR) and then the cells were sequentially exposed to
469 various compounds to assess mitochondrial electron transport chain function (Figures 7A-7C).
470 Our results showed that loss of *Nmp4* elevated basal respiration, maximal respiration, and ATP
471 production in MSPCs (Figures 7A-7C). Spare respiratory capacity and non-mitochondrial
472 respiration were also significantly elevated (data not shown). We conclude that metabolic
473 reprogramming occurs in MSPCs as a consequence of *Nmp4* loss, enhancing the capacity of
474 these cells for oxidative phosphorylation.
475
476 *Nmp4*$^{-/-}$ *osteoprogenitors exhibit enhanced protein production and secretion*

IPA analysis predicted that loss of *Nmp4* elevates the activity of several cellular pathways driving protein production and delivery. Specifically, the activities of the eIF-2 ($z = +3.28^{Day3}; +2.72^{Day7}$), mTOR ($z = +2.949^{Day3}; +2.71^{Day7}$), and the eIF4 and p70SK6 ($z = +3.16^{Day3}; +2.56^{Day7}$) signaling pathways were predicted to be upregulated in *Nmp4*$^{-/-}$ cells (Figure 2, Tables S3 and S4). This suggests that loss of *Nmp4* stimulates anabolic processes including protein synthesis, translation initiation, and the regulation of energy production in mitochondria (71, 105). Loss of *Nmp4* was projected to alter the tRNA signaling pathway but the direction of change could not be predicted ($z = NaN^{Day7}$) (Figure 2; Table S4). Nevertheless, several genes of this pathway were significantly upregulated (Figures 2B & 8). Indeed the expression of numerous genes comprising the pathways of amino acid transport, amino acid biosynthesis, ribosome biogenesis, and translation initiation were significantly elevated (Figure 8). Elevated protein production in *Nmp4*$^{-/-}$ MSPCs is also supported by our earlier report that enhanced ribosome biogenesis was sustained during induction of the unfolded protein response (UPR) which serves to expand the processing capacity of the ER for nascent secretory proteins (25, 114). This Nmp4-directed transcriptome program may allow a large protein client load to be processed through the endoplasmic reticulum without halting global osteoblast translation or inducing apoptosis (114). Indeed, the RNA-seq analysis confirmed that *Nmp4*$^{-/-}$ MSPCs exhibited elevated expression of several genes UPR pathway (Figure 9) and IPA/MAP analysis predicted that protein-folding activity is elevated and UPR-induced apoptosis is attenuated with loss of *Nmp4* (Figure 9).

We validated the transcriptome data experimentally by measuring bone matrix production and delivery in WT and *Nmp4*$^{-/-}$ osteoprogenitors by comparing the levels of *Col1a1*-mRNA associated with polyribosomes and the levels of collagen protein secretion. WT vs. *Nmp4*$^{-/-}$ cells derived from the littermates ($1957^{WT}/1957^{KO}$) and the WT vs. *Nmp4*$^{-/-}$ cells derived from mice obtained from random litters ($1584L^{WT}/1515RR^{KO}$) were cultured in non-differentiating medium for four days. We observed elevated levels of 40S and 60S ribosomal subunits and 80S

monosomes, and increased polysomes in *Nmp4*$^{-/-}$ MSPCs compared to WT (Figure 10A). The RNA-seq data revealed that total *Col1a1* mRNA expression was elevated in the *Nmp4*$^{-/-}$ cells (Figure 10B). To address whether *Col1a1* mRNA translation accompanied the enhanced global translation, qRT-PCR analysis was performed to quantify the amount the of *Col1a1* mRNA present in the polysome fractions prepared from the WT and *Nmp4*$^{-/-}$ cells (Figure 10C). *Col1a1* mRNA was present in heavy polysomes in both WT and *Nmp4*$^{-/-}$ MSPCs, suggesting efficient translation. However, there was a reproducible increase in *Col1a1* mRNA in the largest fraction 7 in *Nmp4*$^{-/-}$ cells, suggesting more robust *Col1a1* translation in the *Nmp4*-depleted cells (Figure 10C). Thus the combination of more *Col1a1* mRNA available for translation, along with increased amounts of ribosomes and more efficient *Col1a1* mRNA translation, would culminate in elevated synthesis of *Col1A1* protein in the *Nmp4*$^{-/-}$ cells.

Collagen deposition is coupled to osteogenic proliferation (78) and *Nmp4*$^{-/-}$ MSPCs frequently exhibit a modest but significant increase in proliferative activity compared to WT (16). To evaluate changes in collagen production induced by *Nmp4* deletion, independent of the confounding effects of proliferation differences, we first measured collagen production in the 1515RR^{KO} and 1584L^{WT} preparations that normally do not exhibit a difference in proliferation. \1515RR^{KO} cells produced approximately 3-4-fold more collagen/cell than the 1584L^{WT} (Figure 10D). Next we evaluated the amount of collagen recovered/well as a function of the number of cells/well for all six MSPC preparations (Figure 10E). All three *Nmp4*$^{-/-}$ preparations produced more collagen compared to WT cells regardless of cell number during this proliferative period in culture (Figure 10E). Moreover, preliminary experiments with shRNA knockdown of *Nmp4* in MC3T3-E1 cells yielded a similar Collagen/well vs. Cells/well profile (data not shown). This is consistent with our previous *in vivo* data showing that the *Nmp4*$^{-/-}$ mice harbor more bone marrow osteoprogenitors than WT, which in turn produce more bone when stimulated (16, 41, 95). We conclude that loss of *Nmp4* converts osteoprogenitors/osteoblasts into super-secretors of bone matrix while moderately enhancing their proliferative activity.

Nmp4$^{-/-}$ *osteoblasts produce a bone matrix with improved material properties*

Several genes representing multiple protein classes comprising the bone matrix (6, 14, 17, 51, 69) were identified as upregulated in our RNA-seq dataset suggesting enhanced matrix material properties in the null animal. The mRNA expression of this collection of genes is represented by a heatmap that displays changes between the *Nmp4*$^{-/-}$ and WT MSPCs/osteogenic cells (Figure 11). Loss of *Nmp4* significantly increased or decreased the expressions and relative ratio of several extracellular matrix (ECM) genes including those that support bone mechanical properties e.g. *Col1a1*, *Col1a2*, *Bglap2* (osteocalcin), and *Spp1* (osteopontin) (Figure 11). Also the expression of key genes that control mineralization were altered in the *Nmp4*$^{-/-}$ cells consistent with the phenotype observed in culture. For example, the genes phosphoethanolamine/phosphocholine phosphatase (*Phospho1*) and alkaline phosphatase, tissue-nonspecific isozyme (*Alpl*), encoding phosphatases responsible for initiating mineralization (5, 43, 67, 112, 113), were highly induced in the *Nmp4*$^{-/-}$ cells as was the gene *Slc20a1* a sodium-phosphate symporter also involved in the initiation of skeletal mineralization (112) (Figure 11). Finally, the expression of several small leucine-rich proteoglycans (SLRPs) such as lumican (*Lum*) and decorin (*Dec*) were highly elevated in the *Nmp4*$^{-/-}$ cells (Figure 13). SLRPs play significant structural roles within the ECM and regulate collagen fibril growth, organization and ECM assembly (12, 47, 76).

To test the biological ramifications of the transcriptional changes associated with the bone matrix genes, we evaluated skeletal tissue obtained from healthy virgin mice that had been treated with the osteoporosis therapeutics RAL, PTH, PTH+RAL and vehicle-control for 7 weeks as described in the Materials and Methods. Ovariectomized mice were not used in this experiment because ovariectomy does not change the enhanced response to anabolic drugs in the *Nmp4*$^{-/-}$ animals (16). Furthermore, all the MSPCs used in this study were derived from healthy, virgin mice. Briefly, μCT analysis showed that the PTH+RAL therapy produced more

555 bone compared to both the PTH and RAL mono-therapies at the distal femur and L5 vertebra
556 (Figures 12A & 12B, Tables 1 and 2). There was a synergistic (greater than additive) interaction
557 between PTH and RAL in both the WT and *Nmp4*$^{-/-}$ mice for BV/TV of the distal femur and the
558 L5 vertebra (Table 2). However, loss of *Nmp4* significantly improved the femoral bone gain and
559 the L5 bone gain in the PTH and PTH+RAL treatments (Figures 12A & 12B Table 1). *Nmp4*
560 status had no impact on bone response to RAL mono-therapy (Figures 12A & 12B, Table 1).
561 Finally, there was no significant difference between the genotypes under the VEH control
562 treatment with respect to femoral and L5 BV/TV (Figures 12A & 12B, Table 1). However loss of
563 *Nmp4* did significantly impact some aspects of femoral cortical geometry, such as cortical
564 thickness, marrow area as well as other related parameters (Table 3). Altogether, these results
565 are similar to the data we reported in older ovariectomized mice (95).

566 A key component of these functional investigations required the measurement of
567 material and structural mechanical properties of the bone. Therefore the left femurs from each
568 animal were monotonically tested to failure. The *Nmp4*$^{-/-}$ bones exhibited a significantly higher
569 ultimate stress, which is the stress necessary to fracture the bone at the material-level,
570 normalized for the bone geometry (Figure 12C, Table 4). Yield stress, the stress applied to the
571 bone after which there is permanent damage, normalized for geometry, was also significantly
572 higher in the *Nmp4*$^{-/-}$ femurs (Figure 12D, Table 4). Additionally, the higher value for the elastic
573 modulus, a measure of the material's stiffness, in *Nmp4*$^{-/-}$ bones approached significance
574 (genotype $p<0.06$, Table 4). Interestingly, numerous material properties were sensitive to the
575 osteoporosis therapies. PTH+RAL led to significantly higher ultimate stress over RAL and PTH
576 mono-therapies in both genotypes (treatment $p<0.0001$ Figure 12C and Table 4). PTH
577 treatment led to a modest but significantly lower yield stress than VEH control and RAL cohorts,
578 which were equivalent. The lower yield stress in the PTH cohorts is likely due to the increased
579 amount of new and less mineralized bone. This would make the tissue less stiff, which is
580 consistent with the modulus trending lowest in the PTH-treated mice (Table 4).

Finally, total strain, elastic modulus, and resilience were all differentially responsive to the various therapies (treatment $p<0.05$ Table 4).

Loss of *Nmp4* also altered the structural properties of the femur. Yield force was significantly increased in the *null* bone (genotype $p=0.004$ Table 5) and the increase in ultimate force neared significance (genotype $p=0.07$). Total displacement, the total amount of deformation the bone undergoes before failure, was significantly lowered in the *Nmp4*$^{-/-}$ femurs (genotype $p=0.04$ Table 5) and the decrease in post yield displacement, the amount of deformation that occurs after the yield point, approached significance ($p=0.06$, Table 5). Finally, work-to-yield, the energy that goes in to deforming the sample was significantly higher in the *Nmp4*$^{-/-}$ bone (genotype $p=0.03$ Table 5). These results show that the *Nmp4*$^{-/-}$ osteoblast produces more matrix than WT cells and that the composition of the secretome results in improved bone material and structural properties.

DISCUSSION:

We investigated the mechanisms underlying the hyper-anabolic phenotype of *Nmp4*$^{-/-}$ MSPCs during osteogenesis. Transcriptomic data predicted that *Nmp4*$^{-/-}$ osteogenic cells have (i) a significantly increased capacity for metabolic conversion to glycolysis, (ii) increased *Col1a1* mRNA translation, (iii) elevated collagen secretion, and (iv) elaborate a matrix that improves bone material and structural mechanical properties. In each case, we were able to anchor the predicted phenotype with experimental results. Moreover the derived mechanistic insights on Nmp4 control of bone cell phenotype were remarkably consistent between the multiple model systems used in this investigation including MSPCs, MC3T3-E1 osteoblast-like cells, and the *in vivo* bone studies. Nevertheless, additional model systems are required to explore Nmp4 control of bone phenotype, e.g. conditional knockout mice and CRISPR cell lines, and we are currently developing these reagents.

The *Nmp4*$^{-/-}$ MSPCs have a significantly increased capacity for metabolic conversion to glycolysis, which is a key driver of osteoblast anabolism. Our ChIP-seq and RNA-seq data show that Nmp4 directly targets and regulates key genes that direct the cell towards aerobic glycolysis including *Pdk1* and *Pkm*. Glucose is a key nutrient for osteoblasts and aerobic glycolysis is the dominant mode of glucose utilization in these cells (49, 53). Thus, while it is a less efficient source of energy, glycolysis can generate both anabolic growth intermediates and ATP very rapidly owing to the much higher speed of glycolysis reactions (97). *In vivo*, PTH-induced bone anabolism is driven in part by the hormone mobilizing osteoblast autocrine IGF1 signaling. This activates mTORC2, which suppresses glucose entry into the TCA cycle and shunts it into the aerobic glycolysis pathway (28). Concomitantly, PTH downregulates Sost/sclerostin expression in osteocytes, unleashing the anabolic WNT signaling pathway (98), driving osteogenesis in part by further stimulating glycolysis via the rapid increase in GLUT1 and HK2 protein expression and escalation in LDHA and PDK1 activities thus increasing glucose consumption and driving lactate over acetyl-CoA production from pyruvate (27).

Our transcriptome data identify the HIF1α and PTEN canonical pathways as significantly sensitive to the status of *Nmp4*, which is consistent with the glycolytic phenotype of the *null* cells. Like the IGF1 and WNT pathways the HIF1α and PTEN link osteogenesis and metabolic reprogramming. Stabilization of the transcription factor HIF1α in Sp7-positive cells in postnatal mice significantly stimulated trabecular bone formation via an increase in the number of osteoblasts and also promoted bone glycolysis via the mRNA upregulation of key glycolytic enzymes including *Pdk1*, *Ldha,* and *Hk2* (85). Mice expressing the stable-oxygen form of HIF1α in osteoprogenitors exhibited an expanded pool of these cells and elevated trabecular BV/TV, very reminiscent of the *Nmp4*$^{-/-}$ skeletal response to PTH (16, 41, 95). Our pathway analysis predicted that PTEN signaling is attenuated in the *Nmp4*$^{-/-}$ cells. Interestingly, PTEN signaling antagonizes the Pi3k-Akt-mTORC2-p70s6k pathway and thus decreases the glycolytic rate and favors oxidative phosphorylation (77). Specifically, PTEN decreases the levels of two key

633 enzymes involved in the Warburg effect, PKM2 and PFKFB3 (33). Therefore, conditional loss of
634 *Pten* in osteoprogenitors led to increased numbers of osteoblasts and expanded bone matrix
635 (35), whereas conditionally disabling *Pten* in mature osteoblasts enhanced mTOR activity and
636 increased bone mineral density (60). Again, this *Pten*-deficient bone phenotype is similar to the
637 *Nmp4*$^{-/-}$ skeleton under PTH challenge.

638 The *Nmp4*$^{-/-}$ MSPCs also exhibited an enhanced capacity for oxidative phosphorylation.
639 This is consistent with a recent study showing that non-differentiated MC3T3-E1 osteoblast-like
640 cells exhibited both spare glycolytic and oxidative capacities (34). Additionally, this study
641 reported that differentiated MC3T3-E1 cells met ATP demand primarily by aerobic glycolysis,
642 whereas non-differentiated cells generated ATP through oxidative phosphorylation (34). Further
643 studies with our MSPCs are required to elucidate the impact of *Nmp4* on metabolic
644 reprogramming during differentiation.

645 The present study revealed that *Nmp4*$^{-/-}$ MSPCs exhibited increased *Col1a1* mRNA
646 translation attendant with elevated collagen secretion revealing part of the mechanism by which
647 these cells are converted into super-secretors. Collagen comprises over 90% of the bone
648 protein matrix and our results suggest that a large percent of *Col1a1* mRNA transcripts are
649 present in the heavy polysomes in *Nmp4*$^{-/-}$ MSPCs implying a high translation of *Col1a1*
650 transcript. This is consistent with our observed increase in collagen protein secretion in these
651 cells. Osteoprogenitor loss of *Nmp4* not only redirects metabolic programming toward cellular
652 anabolism, but also elevates gene expression for multiple pathways involved in protein
653 synthesis and delivery, a key step in bone formation (27, 48). Our transcriptomic analysis
654 showed a striking increase in the mRNA expression of several genes that promote protein
655 anabolism during osteoblast differentiation including numerous amino acid transporters, the
656 amino acid synthase *Asns* and several other genes involved in amino acid synthesis, many
657 tRNA-charging enzymes, and multiple genes driving protein translation initiation as part of the
658 eif4 and eif2 pathways. The present data are consistent with our previous study showing that

659 *Nmp4*$^{-/-}$ MSPCs exhibited significantly elevated ribosome biogenesis, the primary determinant of
660 translational capacity and a key driver of cell growth (114).

661 Another key finding of the present work is that *Nmp4*$^{-/-}$ osteoblasts elaborate a matrix
662 that improves bone material and structural mechanical properties. The expression of matrix
663 genes that contribute to material and structural mechanical properties, e.g. collagen, osteocalcin,
664 and SLRPs were elevated in *Nmp4*$^{-/-}$ cells and mechanical analysis of femurs from mice treated
665 with osteoporosis therapies confirmed enhanced improvement in several of these key properties
666 in the *Nmp4*$^{-/-}$ bone. Enhanced and accelerated mineralization *in vitro* often does not correlate
667 with positive effects on the skeleton. For example, osteoblasts deficient in the expression of
668 *Naca (66)*, *Sox8 (93)*, or *Foxc1 (42)* showed an *ex vivo* accelerated mineralization phenotype;
669 however animals harboring deficits in any one of these genes exhibited significant defects in
670 bone development, formation, or mineralization (42, 66, 93). Sodium fluoride (NaF) is an
671 osteoanabolic that increases bone mass but the newly formed bone lacks normal structure and
672 strength (10, 86, 99). Mechanical load is a bone anabolic signal and the magnitude of the
673 applied strain determines whether the response is adaptive, forming primarily lamellar bone, or
674 injury, producing woven bone (65). Although woven bone forms faster than lamellar bone, it has
675 inferior mechanical and material properties (8, 19). These findings are in stark contrast to our
676 present model in which the precocious and enhanced mineralization of the *Nmp4*$^{-/-}$ osteoblast
677 directly translates into an improved skeletal response to osteoanabolics (15, 16, 41, 95).

678 The molecular mechanisms underlying the improved *Nmp4*$^{-/-}$ bone quality remains to be
679 determined but the enhanced expression of osteocalcin by pharmacologically induced *Nmp4*$^{-/-}$
680 osteogenic cells (15, 16, 95) may improve the quality of the produced bone. Earlier we proposed
681 that non-collagenous proteins act as “glue” at the collagen-mineral interface to resist the
682 separation of the mineralized fibrils and therefore enhance bone toughness (69, 75, 84, 100).
683 Anabolic therapies that induce the formation of osteocalcin/osteopontin-enriched bone may
684 further enhance energy absorption capacity of bone tissue. Therefore loss of *Nmp4* may

685 modestly alter the ratio of collagen to non-collagenous protein matrix composition, which would
686 be enough to improve bone quality. Additionally, the present data suggest that *Nmp4*$^{-/-}$ matrix is
687 enriched in SLRPs, which govern ECM assembly via regulation of linear/lateral fibril growth by
688 binding to the collagen fibril surface (12, 47, 76). Thus the collagen maturation may be
689 accelerated in *Nmp4*$^{-/-}$ bone.

690 The present data demonstrate that Nmp4 acts cell autonomously as a barrier to bone
691 matrix production and mineralization. As an apex regulator of bone cell anabolic output Nmp4
692 directly and indirectly regulates gene programs that control key stages of matrix production and
693 secretion and the metabolic reprogramming necessary to fuel it (Figure 13). The Nmp4
694 transcriptional modus operandi is reminiscent of another apex regulator c-Myc, which like Nmp4
695 controls the expression of large sets of genes involved in ribosome biogenesis, metabolism, and
696 protein synthesis, representing a cell-type-independent genetic program involved in biomass
697 accumulation (38, 45). Furthermore, whereas c-Myc acts a general amplifier of gene expression
698 (50, 73, 108), Nmp4 appears to act as a general attenuator and suppressor of biomass accrual
699 (16, 114). Both the MSPC RNA-seq and Nmp4 MC3T3-E1 ChIP-seq pathway analyses (16) are
700 consistent with this mechanistic profile. Like c-Myc, Nmp4 may directly govern the expression of
701 master transcriptional regulators of these key networks in addition to broadly engaging some of
702 their downstream target genes. Whether there is a functional relationship between c-Myc and
703 Nmp4 remains to be determined. Nmp4 control of protein translation and movement through the
704 bone cell ER is particularly intriguing since this is a potential promising area for drug target
705 discovery. Several therapeutic strategies and multiple drugs are currently being developed to
706 enhance the adaptive capability of the ER in the service of secretion for numerous diseases
707 including diabetes, cancer, Alzheimer's, and osteoporosis (24, 36, 40, 54, 87, 91, 104). Nmp4
708 control of metabolic reprogramming may also present therapeutic targets for regulating bone
709 anabolism (48, 49, 106).

There is a critical medical need for understanding the intrinsic barriers to pharmacologically inducing bone formation in the osteoporotic skeleton (21). Interrogating these pathways may alleviate the current limits to osteoanabolic therapy.

Acknowledgements: We thank Selene Hernandez-Buquer, Jeanette N. McClintick, Chris Wellbrook for their technical assistance. The content is solely the responsibility of the authors and does not necessarily represent the official views of the Department of Defense (DOD), Indiana Clinical and Translational Science Institute (CTSI), or the National Institutes of Health (NIH). This work was supported, in whole or in part, by DOD Grant PR120563; NIH AR070144 and Indiana University School of Medicine CTSI Biomedical Research Grant (to J.P.B.); and NIH Grants AR067221 (to J.M.W.), AR062002 (to M.R.A.), GM049164 (to R.C.W.), AR053237 (to A.G.R.) and NS098772 (to N.B.).

FIGURES AND FIGURE LEGENDS:

Figure 1: Loss of *Nmp4* accelerates and enhances MSPC mineralization and has a broad impact on the transcriptome. **[A]** Six independently expanded MSPC preparations from individual WT and *Nmp4*$^{-/-}$ mice were established as described in Materials and Methods. Cultures were stained with alizarin red when mineralization was first observed. The cells derived from the *Nmp4*$^{-/-}$ mice consistently exhibited mineral days to weeks before this was observed in the WT cultures. The cell preparations 1957N^{KO} and 1957R^{WT} were derived from male littermates. The remaining lines were derived from male or female mice selected from random litters. **[B]** Volcano plots of RNA-seq data from MSPCs maintained in non-differentiating culture medium for 3 days and osteogenic differentiating culture medium for 7 days. The X-axis represents the logarithmic transformation to the base 2 of the mean fold-change of mRNA expression in *Nmp4*$^{-/-}$ cells versus control cells and the Y-axis represents the negative logarithm to the base 10 of the FDR value. Changes in gene expression were considered significant if the fold-change of KO/WT ≥+2 (red circles) and FDR ≤0.05 or KO/WT≤ -2 (green circles) and FDR ≤0.05. The black circles represent genes that did not meet either criteria. The dotted line demarcates FDR=0.05. **[C]** Venn diagrams showing gene overlap between ChIP-seq and RNA-seq data. The former was derived from MC3T3-E1 cells (16). Genes that supported Nmp4 occupancy were required to exhibit peaks (height ≥ 10) within-5 to+2 kb from a transcription start site (TSS) and/or located within the range defined by the TSS and the transcription end site.

Figure 2: Ingenuity Pathway Analysis of the RNA-seq data identified over 200 pathways significantly altered in the *Nmp4*$^{-/-}$ cells maintained in differentiation culture medium for 7 days (see Table S4). Here we show select canonical pathways that are sensitive to *Nmp4* status and relevant to the metabolic reprogramming, protein synthesis and secretion of the bone cells. **[A]** The bar graphs are color-coded to reflect the z-score calculated by the IPA algorithm, which predicts the direction of change for the pathway upon loss of *Nmp4*. An absolute z-score of 2 or

more is considered significant. The activation state of the pathway is predicted to be increased if the z-score is ≥ 2 and these bars are color coded with an orange hue. Conversely, bar graphs with a blue hue indicate a z-score ≤ −2 representing canonical pathways with a decreased activity. Those pathways represented with a grey bar (z = NaN) indicate that the z-score algorithm cannot predict whether the pathway activity is increased or decreased in the *Nmp4*$^{-/-}$ cells. The orange, line gives the ratio of the number of genes listed in the Nmp4 dataset over the total number of genes in the IPA annotated pathway. **[B]** The bar graphs are color coded to reflect the percentage of genes in a particular pathway whose expressions are significantly upregulated with the loss of *Nmp4* (red) and those genes whose expressions are attenuated in the *null* cells (green). The total numbers of genes comprising the canonical pathways are also indicated. The orange line gives the $-\log_{10}$(p-value) and significance was defined by p value≤0.05 [or 1.30= $-\log_{10}$(p-value)].

Figure 3: The IPA Molecule Activity Predictor (MAP) algorithm indicated that loss of *Nmp4* elevates Wnt/β-catenin activity, a major driver of bone anabolism and suppressor of adipogenesis. Molecules in pink-red are found in the dataset and are upregulated. Molecules that are green are found in the dataset and are downregulated. Molecules that are grey are found in the dataset but did not pass any of the filter parameters originally established for the analysis. White molecules are not in the dataset but part of the pathway. Orange molecules and arrows predict activation whereas blue molecules and arrows predict inhibition. On the left-hand side of this pathway is a heatmap of genes comprising the Wnt/β-catenin pathway derived from the RNA-seq data of WT and *Nmp4*$^{-/-}$ MPSCs at Day 3 (uncommitted) and Day 7 (early osteogenesis) in culture. Red boxes indicate increased expression in the *Nmp4*$^{-/-}$ cells compared to the WT, with greater color saturation indicating higher expression, and green indicate reduced expression. The star ✯ indicates Nmp4 binds proximal to the transcription start

site or within the intron of the gene as determined by ChIP-seq analysis (Childress et al., 2015). Abbreviations for the IPA/MAP: Adenomatous polyposis coli protein (APC); B-cell lymphoma 9 (BCL9); the histone acetyl transferase (CBP); Casein kinase I (CKI); Dickkopf (Dkk); disheveled (Dsh); Glycogen synthase kinase 3β (GSK3β); and GSK3 binding protein (GBP); mitogen-activated protein kinase kinase kinase kinase 1 (Hpk1 a.k.a. Map4k1); NEMO-like kinase (NLK); retinoic acid receptor (RAR); nuclear receptor subfamily 2, group C, member 2 (Tak1 a.k.a. Nr2c2); T cell activation factor (TCF).

Figure 4: Loss of *Nmp4* biases the MSPC transcriptome toward the osteogenic lineage. Heatmap of RNA-seq data from WT and *Nmp4*$^{-/-}$ MPSCs at Day 3 (uncommitted) and Day 7 (early osteogenesis) in culture. Red boxes indicate increased expression in the *Nmp4*$^{-/-}$cells compared to the WT, with greater color saturation indicating higher expression, and green indicate reduced expression. The star ✯ indicates Nmp4 binds proximal to the transcription start site or within the intron of the gene as determined by ChIP-seq analysis (16). Also shown, IPA canonical pathways and z scores that support osteogenesis. Orange ovals indicate pathways that are predicted to be activated and whereas blue ovals predict that the pathways are inhibited.

Figure 5: Loss of Nmp4 perturbs the MSPC glycolytic pathway. **[A]** *Nmp4*$^{-/-}$ osteoprogenitors/osteoblasts exhibit significant elevated expression of several genes that drive glycolysis. Schematic of glycolysis/oxidative phosphorylation [OXPHOS] pathways with overlay of heatmap derived from RNA-seq data generated from WT and *Nmp4*$^{-/-}$ MPSCs harvested at Day 3 (uncommitted cells) and Day 7 (early osteogenesis). Red boxes indicate increased expression in the *Nmp4*$^{-/-}$ cells compared to the WT cells, with greater color saturation indicating higher expression, and green color indicates reduced expression. The star ✯ indicates Nmp4 binds proximal to the transcription start site or within the intron of the gene as determined by ChIP-seq analysis (16). **[B]** ChIP-seq reveals Nmp4 binding profiles at specific gene loci in

mouse MC3T3-E1 cells (Childress et al., 2015, GEO accession number GSE112693 for complete ChIP-Seq dataset). The Burrows-Wheeler algorithm was used to align sequences (50-nt reads, single end) to the mouse genome (mm10). Alignments were extended in silico at their 3'-ends to a length of 150bp, which is the average genomic fragment length in the size-selected library, and assigned to 32-nt bins along the genome. The MACS algorithm (v1.4.2) with a cutoff of P = 1e-7 was used to determine Nmp4 (Znf384) peak locations. The genomic loci including the chromosome number and nucleotide interval are indicated. The y-axis indicates the read scales. Arrows indicate the transcriptional start sites and direction of transcription; vertical boxes within the gene indicate exons. The Nmp4 ChIP-seq gene profiles include *Pdk1 Pkm*. The input DNA profiles were devoid of peaks.

Figure 6: Loss of *Nmp4* enhances glycolytic capacity. The line graphs show a comparison of WT vs. *Nmp4*$^{-/-}$ MSPC extracellular acidification rate (ECAR) profiles that have undergone the Glycolytic Stress test. **[A]** The MSPCs 1957R^{WT} and 1957N^{KO} were derived from male littermates. **[B]** The MSPCs 1584L^{WT} and 1515RR^{KO} were derived from a random pair of male WT and *Nmp4*$^{-/-}$ mice. These graphs are representative of 4 individual tissue culture experiments (biological replicates). **[C]** These graphs represent data from 5 separate experiments with cells from 5 different platings. In each experiment, 10 technical replicates with each cell preparation have been performed. The data are mean ± SD. Statistical significance was set at $p<0.05$. Glycolysis is the increase in ECAR measured after the glucose injection. This is the rate of glycolysis under basal conditions. Glycolytic capacity is the increase in ECAR after oligomycin injection. Glycolytic reserve is determined after 2-deoxy-glucose (2-DG) injection, which inhibits glycolysis. The difference between Glycolytic Capacity and Glycolysis rates defines Glycolytic Reserve.

Figure 7: Loss of *Nmp4* enhances mitochondrial respiratory capacity. The line graphs show a comparison of WT vs. *Nmp4*$^{-/-}$ MSPC oxygen consumption rate (OCR) profiles that have undergone the Mitochondrial Stress test. **[A]** The MSPCs 1957R^{WT} and 1957N^{KO} were derived from male littermates. **[B]** The MSPCs 1584L^{WT} and 1515RR^{KO} were derived from a random pair of male WT and *Nmp4*$^{-/-}$ mice. These graphs are representative of 5 individual tissue culture experiments (biological replicates). **[C]** These graphs represent data from 5 separate experiments with cells from 5 different platings. In each experiment, 10 technical replicates with each cell preparation have been performed. The data are mean ± SD. Statistical significance was set at $p<0.05$. Basal respiration (BASAL RESP) was first measured and then the cells were sequentially exposed to various inhibitors of the mitochondrial electron transport chain. ATP production (ATP PROD) was based on the comparison between the basal OCR and the oligomycin-induced drop in OCR. The subsequent injection of carbonyl cyanide-4 (trifluoromethoxy) phenylhydrazone (FCCP) uncoupled the electron transport chain increasing OCR and permitting the calculation of the maximal respiration rate (MAX RESP). Non-mitochondrial respiration was determined from the final injection of rotenone, a complex I inhibitor, and antimycin A, a complex III inhibitor. This parameter was significantly higher in the *Nmp4*$^{-/-}$ cells (data not shown). Spare respiratory capacity was also significantly elevated (data not shown).

Figure 8: Genes involved in various aspects of protein synthesis are shown in the heatmaps positioned along this cellular process. These heatmaps were derived from RNA-seq data generated from WT and *Nmp4*$^{-/-}$ MPSCs harvested at Day 3 (uncommitted cells) and Day 7 (early osteogenesis). Red boxes indicate increased expression in the *Nmp4*$^{-/-}$ cells compared to the WT cells, with greater color saturation indicating higher expression, and green color indicates reduced expression. The star ✯ indicates Nmp4 binds proximal to the transcription start site or within the intron of the gene as determined by ChIP-seq analysis (16).

Figure 9: The IPA Molecule Activity Predictor (MAP) algorithm indicated that loss of *Nmp4* elevates protein folding and attenuates endoplasmic reticulum stress-induced apoptosis. Molecules in pink-red are found in the dataset and are upregulated. Molecules that are green are found in the dataset and are downregulated. Molecules that are grey are found in the dataset but did not pass any of the filter parameters originally established for the analysis. White molecules are not in the dataset but part of the pathway. On the right-hand side of this pathway is a heatmap of genes comprising the unfolded protein response pathway (UPR) derived from the RNA-seq data of WT and *Nmp4*$^{-/-}$ MPSCs at Day 3 (uncommitted) and Day 7 (early osteogenesis) in culture. Red boxes indicate increased expression in the *Nmp4*$^{-/-}$ cells compared to the WT, with greater color saturation indicating higher expression, and green indicate reduced expression. The star ✯ indicates Nmp4 binds proximal to the transcription start site or within the intron of the gene as determined by ChIP-seq analysis. Abbreviations for the IPA/MAP: Autocrine motility factor receptor (AMFR); ER-degradation-enhancing-α-mannidose-like protein (EDEM); ER-associated protein degradation (ERAD); Membrane bound transcription factor peptidase (MBTPS); protein disulfide isomerase (PDI); SREBF chaperone (SCAP); Valosin-containing protein (VCP).

Figure: Loss of *Nmp4* enhances collagen expression and secretion. Data were derived from MSPC preparations 1584L^{WT}, 1515RR^{KO}, 1957R^{WT}, 1957N^{KO} **[A]** Polysome profiles of lysates prepared from WT and *Nmp4*$^{-/-}$ MSPCs at 4 days in culture. Representative profiles from 3 biological replicates **[B]** *Col1a1* mRNA expression as determine by RNA-seq in MSPCs maintained in non-differentiation medium for 3 days in culture and 7 days in culture (5 days in osteogenic medium). **[C]** Following polysome profiling, fractions 1-7 were collected, and the percentage of *Col1a1* mRNA present in each sucrose gradient fraction were quantified by qRT-PCR and presented as a histogram. Data is representative of 2 biological replicates and 3

technical replicates each. Statistical analyses were performed using 1W ANOVA tests and asterisks*** was equivalent to p<0.0001. **[D]** Secretion of collagen protein was measured in the acid-soluble cell-matrix layer of $1584L^{WT}$ and $1515RR^{KO}$ by using the Sircol Assay as described in Materials and Methods. Loss of *Nmp4* significantly enhanced the amount of collagen protein secreted/cell, * p<0.0001. Data represents 3 biological replicates and 5-6 technical replicates each. **[E]** Secretion of collagen protein was measured in the acid-soluble cell-matrix layer by using the Sircol Assay at Day 4 post-seeding from all MSPC preparations $1584L^{WT}$, $1957R^{WT}$, $2001RL^{WT}$, $1515RR^{KO}$, $1957N^{KO}$, and $1986R^{KO}$ and presented as Collagen/well [µg] vs. cell number/well. All six preparations were tested independently at least twice (Experiments 1 & 2) and experiments comprised 4-6 wells/preparation. All *Nmp4*$^{-/-}$ [KO] preparations produced more collagen during the first four days of culture, regardless of cell number. Data represents average ± SD, n=4-6 wells/group.

Figure 11: *Nmp4*$^{-/-}$ osteoprogenitors/osteoblasts exhibit significant elevated expression of several genes that encode proteins of the bone matrix. The schematic shows family of proteins that comprise the bone matrix. Also the expressions of key genes that control mineralization were altered in the *Nmp4*$^{-/-}$ cells consistent with the observed phenotype observed in culture. The manually annotated heatmap was derived from RNA-seq data generated from WT and *Nmp4*$^{-/-}$ MPSCs harvested at Day 3 (uncommitted cells) and Day 7 (early osteogenesis). Red boxes indicate increased expression in the *Nmp4*$^{-/-}$ cells compared to the WT cells, with greater color saturation indicating higher expression, and green color indicates reduced expression. The star ✯ indicates Nmp4 binds proximal to the transcription start site or within the intron of the gene as determined by ChIP-seq analysis (16).

Figure 12: Loss of *Nmp4* improves enhances therapeutically induced bone formation and femoral material properties. **[A]** Femoral and **[B]** L5 vetebral BV/TV for all the experimental

cohorts (age 17wks) comparing WT and *Nmp4*$^{-/-}$ mice. We compared the therapies RAL, PTH, and PTH+RAL to each other and to VEH. Statistical analyses were performed using 2W ANOVA tests setting genotype and treatment as the independent variables. Statistical significance was set at $p \leq 0.05$. There were a strong genotype effect and loss of *Nmp4* enhanced femoral and L5 vertebral BV/TV over the cohorts. There was a strong treatment effect and PTH+RAL was the most efficacious osteoanabolic therapy for both femoral and L5 vertebral BV/TV. The analysis revealed a genotype x treatment interaction (G x T denoted by an asterisk in the dot plot showing improved response in the PTH mono-therapy and PTH+RAL combination therapy with loss of *Nmp4*. Results of 3pt-bending analysis for **[C]** Ultimate stress **[D]** Yield stress. There were strong genotype and treatment effects for both ultimate stress and yield stress. Data represents average ± SD, n=8-15 mice/group.

Figure 13: Hypothesis—Nmp4 is an apex regulator of bone cell anabolic output. This transcription factor directly and indirectly regulates gene programs that control key stages of matrix production and delivery. It may accomplish this by regulating both the expression of master transcriptional regulators of these pathways in addition to broadly engaging several of their downstream target genes.

TABLES

TABLE 1: FEMORAL AND L5 TRABECULAR ARCHITECTURE

GROUP	Femur BV/TV [%]	Femur Tb N (mm^{-1})	Femur Tb Th (mm)	Femur Tb Sp (mm)
WT VEH	4.57±0.83	0.970±0.163	0.047±0.003	0.282±0.013
Nmp4$^{-/-}$ VEH	6.53±0.93	1.346±0.0.163	0.048±0.002	0.250±0.008
WT RAL	11.13±1.03	1.885±0.146	0.060±0.001	0.245±0.010
Nmp4$^{-/-}$ RAL	13.38±1.37	2.203±0.161	0.061±0.002	0.227±0.011
WT PTH	13.60±3.39	2.265±0.382	0.059±0.005	0.230±0.020
Nmp4$^{-/-}$ PTH	25.30±6.86	3.304±0.592	0.076±0.008	0.190±0.016
WT PTH+RAL	26.37±2.04	3.591±0.355	0.077±0.005	0.194±0.012
Nmp4$^{-/-}$ PTH+RAL	47.82±15.70	5.125±1.316	0.092±0.008	0.139±0.028
2W ANOVA GENOTYPE	**G: p<0.0001** *Nmp4*$^{-/-}$: A 23.26 WT: B 13.92	**G: p<0.0001** *Nmp4*$^{-/-}$: A 2.99 WT: B 2.18	**G: p<0.0001** *Nmp4*$^{-/-}$: A 0.069 WT: B 0.061	**G: p<0.0001** WT: A 0.238 *Nmp4*$^{-/-}$: B 0.201
2W ANOVA TREATMENT	**T: p<0.0001** P+R: A 37.10 P: B 19.45 R: C 12.25 V: D 5.55	**T: p<0.0001** P+R: A 4.36 P: B 2.78 R: C 2.04 V: D 1.16	**T: p<0.0001** P+R: A 0.084 P: B 0.067 R: C 0.062 V: D 0.047	**T: p<0.0001** V: A 0.266 R: B 0.236 P: C 0.210 P+R: D 0.167
2W ANOVA G x T	**G x T: p<0.0001** *Nmp4*$^{-/-}$ P+R: A 47.82 WT P+R: B 26.37 *Nmp4*$^{-/-}$ P: B 25.30 WT P: CD 13.60 *Nmp4*$^{-/-}$ R: C 13.38 WT R: CD 11.13 *Nmp4*$^{-/-}$ R: CD 6.53 WT V: D 4.57	**G x T: p=0.0015** *Nmp4*$^{-/-}$ P+R: A 5.13 WT P+R: B 3.59 *Nmp4*$^{-/-}$ P: B 3.30 WT P: C 2.27 *Nmp4*$^{-/-}$ R: C 2.20 WT R: CD 1.88 *Nmp4*$^{-/-}$ V: DE 1.35 WT V: E 0.97	**G x T: p<0.0001** *Nmp4*$^{-/-}$ P+R: A 0.092 WT P+R: B 0.077 *Nmp4*$^{-/-}$ P: B 0.076 *Nmp4*$^{-/-}$ R: C 0.061 WT R: C 0.060 WT P: C 0.059 *Nmp4*$^{-/-}$ V: D 0.048 WT V: D 0.047	**G x T: p=0.0022** WT V: A 0.282 *Nmp4*$^{-/-}$ V: B 0.250 WT R: BC 0.245 WT P: BC 0.230 *Nmp4*$^{-/-}$ R: C 0.227 WT P+R: D 0.194 *Nmp4*$^{-/-}$ P: D 0.190 *Nmp4*$^{-/-}$ P+R: E 0.139

GROUP	L5 BV/TV [%]	L5 Tb N (mm^{-1})	L5 Tb Th (mm)	L5 Tb Sp (mm)
WT VEH	24.65±2.05	4.37±0.27	0.056±0.002	0.210±0.017
Nmp4$^{-/-}$ VEH	26.56±2.11	4.37±0.22	0.061±0.003	0.204±0.014
WT RAL	28.62±4.10	5.11±0.71	0.056±0.003	0.201±0.027
Nmp4$^{-/-}$ RAL	31.20±2.83	5.24±0.39	0.059±0.003	0.185±0.008
WT PTH	36.26±2.87	6.60±0.30	0.057±0.003	0.161±0.036
Nmp4$^{-/-}$ PTH	40.62±2.23	6.44±0.18	0.062±0.003	0.153±0.016
WT PTH+RAL	48.28±2.72	8.12±0.24	0.061±0.005	0.129±0.003
Nmp4$^{-/-}$ PTH+RAL	55.76±3.02	8.07±0.47	0.071±0.004	0.120±0.013
2W ANOVA GENOTYPE	**G: p<0.0001** *Nmp4*$^{-/-}$: A 38.54 WT: B 34.22	**G: p=0.8545** *Nmp4*$^{-/-}$=WT	**G: p<0.0001** *Nmp4*$^{-/-}$: A 0.063 WT: B 0.057	**G: p=0.0324** WT: A 0.175 *Nmp4*$^{-/-}$: B 0.166
2W ANOVA TREATMENT	**T: p<0.0001** P+R: A 52.02 P: B 38.44 R: C 29.91 V: D 25.61	**T: p<0.0001** P+R: A 8.10 P: B 6.52 R: C 5.17 V: D 4.37	**T: p<0.0001** P+R: A 0.066 P: B 0.059 R: B 0.059 V: B 0.0578	**T: p<0.0001** V: A 0.207 R: A 0.193 P: B 0.157 P+R: C 0.124
2W ANOVA G x T	**G x T: p=0.0133** *Nmp4*$^{-/-}$ P+R: A 55.76 WT P+R: B 48.28 *Nmp4*$^{-/-}$ P: C 40.63 WT P: D 36.26 *Nmp4*$^{-/-}$ R: E 31.20 WT R: EF 28.62 *Nmp4*$^{-/-}$ V: F 26.56 WT V: F 24.65	**G x T: p=0.6648**	**G x T: p=0.0154** *Nmp4*$^{-/-}$ P+R: A 0.071 *Nmp4*$^{-/-}$ P: B 0.062 *Nmp4*$^{-/-}$ V: BC 0.061 WT P+R: BC 0.061 *Nmp4*$^{-/-}$ R: BC 0.059 WT P: C 0.057 WT V: C 0.056 WT R: C 0.056	**G xT: p=0.8336**

TABLE 1: Femoral and L5 trabecular architecture from WT and *Nmp4*$^{-/-}$ mice treated with vehicle (V), raloxifene (R), parathyroid hormone (P), and parathyroid hormone + raloxifene (P+R). Statistical analyses were performed using 2W ANOVA tests setting genotype (G) and treatment (T) as the independent variables. Statistical significance was set at $p \leq 0.05$. The statistical results list the cohorts by genotype, treatment, and genotype x treatment. Cohorts not connected by the same letter are statistically different. The average value of the specific parameter follows the letter. The data represents average ± SD, n=8-15 mice/group. See text for explanation of results.

TABLE 2: PTH and RAL Synergy

THERAPY	p-value PTH Treatment	p-value RAL Treatment	p-value PTH x RAL interaction
FEMUR BV/TV			
PTH+RAL [WT]	p<0.0001	p<0.0001	p<0.0001
PTH+RAL [*Nmp4*$^{-/-}$]	p<0.0001	p<0.0001	0.001
L5 BV/TV			
PTH+RAL [WT]	p<0.0001	p<0.0001	0.0008
PTH+RAL [*Nmp4*$^{-/-}$]	p<0.0001	p<0.0001	p<0.0001
CORTICAL AREA			
PTH+RAL [WT]	<0.0001	0.0591	0.8056
PTH+RAL [*Nmp4*$^{-/-}$]	<0.0001	0.0166	0.5938

TABLE 2: Identification of synergy between PTH and the anti-catabolic SERM RAL using a series of 2 way ANOVA tests comparing the efficacy of the PTH mono-therapy, RAL mono-therapy and the combination of the two drugs. Statistical significance was set at $p \leq 0.05$

TABLE 3: FEMORAL CORTICAL PARAMETERS

GROUP	Marrow Area (mm^2)	Cortical Area (mm^2)	Cortical Thickness (mm)	Periosteal BS (mm)	Endocortical BS (mm)
WT VEH	0.940±0.049	0.829±0.052	0.204±0.008	5.393±0.139	4.140±0.114
Nmp4$^{-/-}$ VEH	0.913±0.049	0.838±0.039	0.209±0.009	5.353±0.090	4.078±0.106
WT RAL	0.860±0.022	0.867±0.037	0.216±0.006	5.344±0.090	4.019±0.095
Nmp4$^{-/-}$ RAL	0.879±0.039	0.865±0.047	0.218±0.010	5.332±0.111	4.004±0.103
WT PTH	0.969±0.048	0.949±0.078	0.221±0.005	5.617±0.196	4.213±0.108
Nmp4$^{-/-}$ PTH	0.931±0.064	0.951±0.062	0.226±0.007	5.564±0.087	4.142±0.116
WT PTH+RAL	0.892±0.043	0.995±0.070	0.239±0.007	5.552±0.152	4.084±0.106
Nmp4$^{-/-}$ PTH+RAL	0.852±0.029	1.00±0.067	0.249±0.013	5.478±0.081	3.978±0.038
2W ANOVA GENOTYPE	**G: p=0.0295** WT A 0.915 *Nmp4*$^{-/-}$: B 0.894	**G: p=0.3420**	**G: p=0.008** *Nmp4*$^{-/-}$: A 0.225 WT: B 0.220	**G: p=0.0780**	**G: p=0.0034** WT A 4.11 *Nmp4*$^{-/-}$: B 4.05
2W ANOVA TREATMENT	**T: p<0.0001** P A 0.950 V: A 0.927 P+R: B 0.872 R: B 0.869	**T: p<0.0001** P+R A 0.990 P: A 0.954 R: B 0.866 V: B 0.833	**T: p<0.0001** P+R: A 0.244 P: B 0.223 R: B 0.217 V: C 0.206	**T: p<0.0001** P: A 5.59 P+R: A 5.52 V: B 5.37 R: B 5.34	**T: p<0.0001** P: A 4.18 V: A 4.11 P+R: B 4.03 R: B 4.01
2W ANOVA G x T	**G x T: p=0.1459**	**G x T: p=0.88**	**G x T: p=0.4695**	**G x T: p=0.8513**	**G x T: p=0.4973**

GROUP	I_{ap} (mm^4)	I_{ml} (mm^4)	I_{max} (mm^4)	I_{min} (mm^4)	TMD (g/cm^3 HA)
WT VEH	0.228±0.029	0.144±0.015	0.237±0.029	0.135±0.015	1.29±0.03
Nmp4$^{-/-}$ VEH	0.219±0.008	0.143±0.012	0.224±0.013	0.137±0.012	0.89±0.01
WT RAL	0.231±0.016	0.144±0.012	0.237±0.016	0.138±0.010	1.27±0.01
Nmp4$^{-/-}$ RAL	0.228±0.021	0.142±0.012	0.235±0.022	0.138±0.014	0.89±0.01
WT PTH	0.285±0.048	0.179±0.022	0.297±0.053	0.167±0.019	1.28±0.03
Nmp4$^{-/-}$ PTH	0.279±0.025	0.173±0.007	0.281±0.022	0.169±0.010	0.89±0.01
WT PTH+RAL	0.291±0.044	0.173±0.016	0.302±0.043	0.162±0.016	1.28±0.02
Nmp4$^{-/-}$ PTH+RAL	0.270±0.030	0.174±0.019	0.276±0.031	0.167±0.017	0.88±0.01
2W ANOVA GENOTYPE	**G: p=0.1257**	**G: p=0.5224**	**G: p=0.0325** WT A 0.268 *Nmp4*$^{-/-}$: B 0.254	**G: p=0.4557**	**G: p<0.0001** WT A 1.28 *Nmp4*$^{-/-}$: B 0.886
2W ANOVA TREATMENT	**T: p<0.0001** P A 0.282 P+R: A 0.281 R: B 0.230 V: B 0.223	**T: p<0.0001** P A 0.176 P+R: A 0.173 V: B 0.143 R: B 0.143	**T: p<0.0001** P+R A 0.289 P: A 0.289 R: B 0.236 V: B 0.230	**T: p<0.0001** P: A 0.168 P+R: A 0.165 R: B 0.138 V: B 0.136	**T: p=0.2325**
2W ANOVA G x T	**G x T: p=0.7276**	**G x T: p=0.9050**	**G x T: p=0.6236**	**G x T: p=0.9269**	**G x T: p=0.3597**

TABLE 3: Femoral cortical architecture from WT and *Nmp4*$^{-/-}$ mice treated with vehicle (V), raloxifene (R), parathyroid hormone (P), and parathyroid hormone + raloxifene (P+R). Statistical analyses were performed using 2W ANOVA tests setting genotype (G) and treatment (T) as the independent variables. Statistical significance was set at p≤0.05. The statistical results list the cohorts by genotype, treatment, and genotype x treatment. Cohorts not connected by the same letter are statistically different. The average value of the specific parameter follows the letter. The data represents average ± SD, n=7-15 mice/group. See text for explanation of results. ABBREVIATIONS: HA hydroxyapatite; I_{ap} moment of inertia about the femoral anterior–posterior length axis; I_{max} maximum moment of inertia; I_{min} minimum moment of inertia; I_{ml} moment of inertia about the femoral medial–lateral axis; TMD tissue mineral density.

TABLE 4: ESTIMATED MATERIAL PROPERTIES

GROUP	Ultimate Stress	Yield Stress	Strain to Yield (με)	Total Strain (με)	Modulus (GPa)	Resilience (MPa)	Toughness (MPa)
WT VEH	141.12±6.97	105.73±12.89	16012±1124	99029±30556	7.87±0.30	0.95±0.18	9.19±1.93
***Nmp4*$^{-/-}$ VEH**	150.08±8.71	121.23±21.47	16982±2858	82378±26470	8.55±0.54	1.08±0.31	8.86±2.59
WT RAL	155.49±5.00	117.92±5.13	16552±371	83863±19659	8.06±0.75	1.06±0.12	9.15±1.86
***Nmp4*$^{-/-}$ RAL**	159.48±13.63	127.00±22.37	16999±2556	75610±19939	8.24±1.13	1.20±0.35	8.95±2.10
WT PTH	152.07±4.20	97.09±15.56	16881±3008	90210±29366	7.57±1.23	0.85±0.28	9.46±2.63
***Nmp4*$^{-/-}$ PTH**	157.94±5.37	97.77±9.56	15021±1932	91519±26401	7.93±0.30	0.82±0.23	10.31±2.28
WT PTH+RAL	166.39±3.78	102.76±18.16	15452±34324	69998±19460	8.44±0.38	0.89±0.32	8.16±1.90
***Nmp4*$^{-/-}$ PTH+RAL**	173.39±10.84	114.52±13.66	15321±708	63635±16321	8.64±1.06	0.99±0.20	8.09±1.91
2W ANOVA GENOTYPE	**G: p=0.0012** Nmp4$^{-/-}$: A 160.22 WT: B 153.77	**G: p=0.0109** Nmp4$^{-/-}$: A 115.13 WT: B 105.87	**G: p=0.7849**	**G: p=0.1310**	**G: p=0.0559**	**G: p=0.1304**	**G: p=0.8913**
2W ANOVA TREATMENT	**T: p<0.0001** P+R: A 169.89 R: B 157.48 P: B 155.00 V: C 145.60	**T: p<0.0001** R: A 122.46 V: AB 113.48 P+R: BC 108.64 P: C 97.43	**T: p=0.2740**	**T: p=0.0016** P: A 90864 V: A 90704 R: AB 79737 P+R: B 66816	**T: p=0.0318** P+R: A 8.54 V: AB 8.21 R: AB 8.15 P: B 7.55	**T: p=0.0031** R: A 1.13 V: AB 1.01 P+R: AB 0.94 P: B 0.84	**T: p=0.0553**
2W ANOVA G x T	**G x T: p=0.8141**	**G x T: p=0.5067**	**G x T: p=0.2220**	**G x T: p=0.6425**	**G x T: p=0.7598**	**G x T: p=0.6545**	**G x T: p=0.7901**

TABLE 4: Estimated femoral material properties from WT and *Nmp4*$^{-/-}$ mice treated with vehicle (V), raloxifene (R), parathyroid hormone (P), and parathyroid hormone + raloxifene (P+R). Statistical analyses were performed using 2W ANOVA tests setting genotype (G) and treatment (T) as the independent variables. Statistical significance was set at p≤0.05. The statistical results list the cohorts by genotype, treatment, and genotype x treatment. Cohorts not connected by the same letter are statistically different. The average value of the specific parameter follows the letter. The data represents average ± SD, n=7-14 mice/group.

TABLE 5: STRUCTURAL MECHANCIAL PROPERTIES

GROUP	Yield force (N)	Ultimate force (N)	Displacement to yield (μm)	Post yield displacement (μm)	Total displacement (μm)
WT VEH	10.08±0.99	13.52±1.16	162.51±12.49	843.05±320.03	1005.56±312.72
Nmp4$^{-/-}$ VEH	11.65±2.44	14.27±0.92	172.64±26.99	619.27±224.97	792.43±217.81
WT RAL	11.19±0.20	14.67±0.41	168.22±12.96	689.72±208.95	861.14±199.79
Nmp4$^{-/-}$ RAL	15.22±1.20	15.22±1.20	173.53±15.73	594.32±202.51	769.68±193.22
WT PTH	11.04±2.06	16.94±1.67	163.51±28.73	711.57±297.33	875.08±288.88
Nmp4$^{-/-}$ PTH	11.24±1.79	17.06±1.38	146.49±18.81	742±255.98	894.10±252.89
WT PTH+RAL	11.50±1.18	18.38±2.31	152.56±34.07	540.96±205.28	693.53±202.12
Nmp4$^{-/-}$ PTH+RAL	13.66±2.51	19.43±2.18	152.09±8.08	458.30±166.36	578.77±109.62
2W ANOVA GENOTYPE	**G: p= 0.0037** *Nmp4*$^{-/-}$: A 12.22 WT: B 10.95	**G: p=0.0680**	**G: p=0.9119**	**G: p=0.0610**	**G: p= 0.0379** WT: A 858.83 *Nmp4*$^{-/-}$: B 758.74
2W ANOVA TREATMENT	**T: p=0.0243** P+R: A 12.58 R: AB 11.76 P: AB 11.14 V: B 10.87	**T: p<0.0001** P+R: A 18.91 P: B 17.00 R: C 14.95 V: C 13.90	**T: p=0.0137** R: A 170.87 V: AB 167.57 P: AB 155.00 P+R: B 152.33	**T: p=0.0028** V: A 731.16 P: A 726.78 R: AB 642.02 P+R: B 499.64	**T: p=0.0005** V: A 898.99 P: A 884.59 R: A 815.41 P+R: B 636.15
2W ANOVA G x T	**G x T: p=0.4051**	**G x T: p=0.7791**	**G x T: p=0.1830**	**G x T: p=0.3475**	**G x T: p=0.3910**

GROUP	Stiffness (N/mm)	Work to Yield (mJ)	Post Yield Work (mJ)	Total Work (mJ)
WT VEH	95.73±6.19	0.92±0.16	8.01±2.16	8.93±2.05
Nmp4$^{-/-}$ VEH	104.39±10.17	1.05±0.31	7.53±2.63	8.64±2.63
WT RAL	106.07±12.65	1.05±0.08	8.10±1.91	9.15±1.90
Nmp4$^{-/-}$ RAL	105.42±16.10	1.19±0.34	7.63±2.14	8.91±2.17
WT PTH	120.02±22.68	0.94±0.32	9.44±2.92	10.38±2.76
Nmp4$^{-/-}$ PTH	121.91±16.51	0.89±0.23	10.24±2.81	11.18±2.74
WT PTH+RAL	130.49±10.66	0.92±0.29	7.98±1.97	8.97±1.85
Nmp4$^{-/-}$ PTH+RAL	132.83±17.91	1.25±0.45	7.69±2.61	8.94±2.45
2W ANOVA GENOTYPE	**G: p= 0.3316**	**G: p=0.0315** *Nmp4*$^{-/-}$: A 1.10 WT: B 0.96	**G: p=0.8291**	**G: p=0.8989**
2W ANOVA TREATMENT	**T: p<0.0001** P+R: A 131.66 P: A 120.97 R: B 105.74 V: B 100.06	**T: p=0.0985**	**T: p=0.0103** P: A 9.84 R: B 7.87 P+R: B 7.83 V: B 7.77	**T: p=0.0159** P: A 10.78 R: AB 9.03 P+R: B 8.95 V: B 8.79
2W ANOVA G x T	**G x T: p=0.7575**	**G x T: p=0.2168**	**G x T: p=0.7762**	**G x T: p=0.8461**

TABLE 5: Estimated femoral structural mechanical properties from WT and *Nmp4*$^{-/-}$ mice treated with vehicle (V), raloxifene (R), parathyroid hormone (P), and parathyroid hormone + raloxifene (P+R). Statistical analyses were performed using 2W ANOVA tests setting genotype (G) and treatment (T) as the independent variables. Statistical significance was set at p≤0.05. The statistical results list the cohorts by genotype, treatment, and genotype x treatment. Cohorts not connected by the same letter are statistically different. The average value of the specific parameter follows the letter. The data represents average ± SD, n=7-14 mice/group.

REFERENCES:

1. **Alford AI, Terkhorn SP, Reddy AB, and Hankenson KD.** Thrombospondin-2 regulates matrix mineralization in MC3T3-E1 pre-osteoblasts. *Bone* 46: 464-471, 2010.
2. **Baird TD, Palam LR, Fusakio ME, Willy JA, Davis CM, McClintick JN, Anthony TG, and Wek RC.** Selective mRNA translation during eIF2 phosphorylation induces expression of IBTKalpha. *Molecular biology of the cell* 25: 1686-1697, 2014.
3. **Bandeira L, Lewiecki EM, and Bilezikian JP.** Romosozumab for the treatment of osteoporosis. *Expert opinion on biological therapy* 17: 255-263, 2017.
4. **Bart ZR, Hammond MA, and Wallace JM.** Multi-scale analysis of bone chemistry, morphology and mechanics in the oim model of osteogenesis imperfecta. *Connective tissue research* 55 Suppl 1: 4-8, 2014.
5. **Bellows CG, Aubin JE, and Heersche JN.** Initiation and progression of mineralization of bone nodules formed in vitro: the role of alkaline phosphatase and organic phosphate. *Bone and mineral* 14: 27-40, 1991.
6. **Boskey AL.** Bone composition: relationship to bone fragility and antiosteoporotic drug effects. *BoneKEy reports* 2: 447, 2013.
7. **Boudin E, Fijalkowski I, Piters E, and Van Hul W.** The role of extracellular modulators of canonical Wnt signaling in bone metabolism and diseases. *Seminars in arthritis and rheumatism* 43: 220-240, 2013.
8. **Buckwalter JA, Glimcher MJ, Cooper RR, and Recker R.** Bone biology. I: Structure, blood supply, cells, matrix, and mineralization. *Instructional course lectures* 45: 371-386, 1996.
9. **Canalis E, Kranz L, and Zanotti S.** Nemo-like kinase regulates postnatal skeletal homeostasis. *Journal of cellular physiology* 229: 1736-1743, 2014.
10. **Carter DR and Beaupre GS.** Effects of fluoride treatment on bone strength. *Journal of bone and mineral research : the official journal of the American Society for Bone and Mineral Research* 5 Suppl 1: S177-184, 1990.
11. **Charoenpanich A, Wall ME, Tucker CJ, Andrews DM, Lalush DS, and Loboa EG.** Microarray analysis of human adipose-derived stem cells in three-dimensional collagen culture: osteogenesis inhibits bone morphogenic protein and Wnt signaling pathways, and cyclic tensile strain causes upregulation of proinflammatory cytokine regulators and angiogenic factors. *Tissue engineering Part A* 17: 2615-2627, 2011.
12. **Chen S and Birk DE.** The regulatory roles of small leucine-rich proteoglycans in extracellular matrix assembly. *The FEBS journal* 280: 2120-2137, 2013.
13. **Chevalier Y, Quek E, Borah B, Gross G, Stewart J, Lang T, and Zysset P.** Biomechanical effects of teriparatide in women with osteoporosis treated previously with alendronate and risedronate: results from quantitative computed tomography-based finite element analysis of the vertebral body. *Bone* 46: 41-48, 2010.
14. **Chiellini C, Cochet O, Negroni L, Samson M, Poggi M, Ailhaud G, Alessi MC, Dani C, and Amri EZ.** Characterization of human mesenchymal stem cell secretome at early steps of adipocyte and osteoblast differentiation. *BMC molecular biology* 9: 26, 2008.
15. **Childress P, Philip BK, Robling AG, Bruzzaniti A, Kacena MA, Bivi N, Plotkin LI, Heller A, and Bidwell JP.** Nmp4/CIZ suppresses the response of bone to anabolic parathyroid hormone by regulating both osteoblasts and osteoclasts. *Calcified tissue international* 89: 74-89, 2011.

16. **Childress P, Stayrook KR, Alvarez MB, Wang Z, Shao Y, Hernandez-Buquer S, Mack JK, Grese ZR, He Y, Horan D, Pavalko FM, Warden SJ, Robling AG, Yang FC, Allen MR, Krishnan V, Liu Y, and Bidwell JP.** Genome-Wide Mapping and Interrogation of the Nmp4 Antianabolic Bone Axis. *Molecular endocrinology* 29: 1269-1285, 2015.
17. **Choi YA, Lim J, Kim KM, Acharya B, Cho JY, Bae YC, Shin HI, Kim SY, and Park EK.** Secretome analysis of human BMSCs and identification of SMOC1 as an important ECM protein in osteoblast differentiation. *Journal of proteome research* 9: 2946-2956, 2010.
18. **Cipriani C, Irani D, and Bilezikian JP.** Safety of osteoanabolic therapy: a decade of experience. *Journal of bone and mineral research : the official journal of the American Society for Bone and Mineral Research* 27: 2419-2428, 2012.
19. **Currey JD.** Mechanical properties of vertebrate hard tissues. *Proceedings of the Institution of Mechanical Engineers Part H, Journal of engineering in medicine* 212: 399-411, 1998.
20. **Dalton LE, Healey E, Irving J, and Marciniak SJ.** Phosphoproteins in stress-induced disease. *Progress in molecular biology and translational science* 106: 189-221, 2012.
21. **Dede AD, Makras P, and Anastasilakis AD.** Investigational anabolic agents for the treatment of osteoporosis: an update on recent developments. *Expert opinion on investigational drugs* 26: 1137-1144, 2017.
22. **Dimmer KS, Friedrich B, Lang F, Deitmer JW, and Broer S.** The low-affinity monocarboxylate transporter MCT4 is adapted to the export of lactate in highly glycolytic cells. *The Biochemical journal* 350 Pt 1: 219-227, 2000.
23. **Dobin A, Davis CA, Schlesinger F, Drenkow J, Zaleski C, Jha S, Batut P, Chaisson M, and Gingeras TR.** STAR: ultrafast universal RNA-seq aligner. *Bioinformatics* 29: 15-21, 2013.
24. **Doultsinos D, Avril T, Lhomond S, Dejeans N, Guedat P, and Chevet E.** Control of the Unfolded Protein Response in Health and Disease. *SLAS discovery*: 2472555217701685, 2017.
25. **Dufey E, Sepulveda D, Rojas-Rivera D, and Hetz C.** Cellular mechanisms of endoplasmic reticulum stress signaling in health and disease. 1. An overview. *American journal of physiology Cell physiology* 307: C582-594, 2014.
26. **Eriksen EF and Brown JP.** Commentary: Concurrent administration of PTH and antiresorptives: Additive effects or DXA cosmetics. *Bone* 86: 139-142, 2016.
27. **Esen E, Chen J, Karner CM, Okunade AL, Patterson BW, and Long F.** WNT-LRP5 signaling induces Warburg effect through mTORC2 activation during osteoblast differentiation. *Cell metabolism* 17: 745-755, 2013.
28. **Esen E, Lee SY, Wice BM, and Long F.** PTH Promotes Bone Anabolism by Stimulating Aerobic Glycolysis via IGF Signaling. *Journal of bone and mineral research : the official journal of the American Society for Bone and Mineral Research* 30: 1959-1968, 2015.
29. **Fox J, Miller MA, Newman MK, Turner CH, Recker RR, and Smith SY.** Treatment of skeletally mature ovariectomized rhesus monkeys with PTH(1-84) for 16 months increases bone formation and density and improves trabecular architecture and biomechanical properties at the lumbar spine. *Journal of bone and mineral research : the official journal of the American Society for Bone and Mineral Research* 22: 260-273, 2007.
30. **Gallacher SJ and Dixon T.** Impact of treatments for postmenopausal osteoporosis (bisphosphonates, parathyroid hormone, strontium ranelate, and denosumab) on bone quality: a systematic review. *Calcified tissue international* 87: 469-484, 2010.

31. **Gallego Romero I, Pai AA, Tung J, and Gilad Y.** RNA-seq: impact of RNA degradation on transcript quantification. *BMC biology* 12: 42, 2014.
32. **Gamsjaeger S, Buchinger B, Zoehrer R, Phipps R, Klaushofer K, and Paschalis EP.** Effects of one year daily teriparatide treatment on trabecular bone material properties in postmenopausal osteoporotic women previously treated with alendronate or risedronate. *Bone* 49: 1160-1165, 2011.
33. **Garcia-Cao I, Song MS, Hobbs RM, Laurent G, Giorgi C, de Boer VC, Anastasiou D, Ito K, Sasaki AT, Rameh L, Carracedo A, Vander Heiden MG, Cantley LC, Pinton P, Haigis MC, and Pandolfi PP.** Systemic elevation of PTEN induces a tumor-suppressive metabolic state. *Cell* 149: 49-62, 2012.
34. **Guntur AR, Gerencser AA, Le PT, DeMambro VE, Bornstein SA, Mookerjee SA, Maridas DE, Clemmons DE, Brand MD, and Rosen CJ.** Osteoblast-like MC3T3-E1 Cells Prefer Glycolysis for ATP Production but Adipocyte-like 3T3-L1 Cells Prefer Oxidative Phosphorylation. *Journal of bone and mineral research : the official journal of the American Society for Bone and Mineral Research*, 2018.
35. **Guntur AR, Reinhold MI, Cuellar J, Jr., and Naski MC.** Conditional ablation of Pten in osteoprogenitors stimulates FGF signaling. *Development (Cambridge, England)* 138: 1433-1444, 2011.
36. **Hamamura K, Tanjung N, and Yokota H.** Suppression of osteoclastogenesis through phosphorylation of eukaryotic translation initiation factor 2 alpha. *Journal of bone and mineral metabolism* 31: 618-628, 2013.
37. **Han HS, Ju F, and Geng S.** In vivo and in vitro effects of PTH1-34 on osteogenic and adipogenic differentiation of human bone marrow-derived mesenchymal stem cells through regulating microRNA-155. *Journal of cellular biochemistry*, 2017.
38. **Hann SR.** MYC cofactors: molecular switches controlling diverse biological outcomes. *Cold Spring Harbor perspectives in medicine* 4: a014399, 2014.
39. **Hawkins KE, Joy S, Delhove JM, Kotiadis VN, Fernandez E, Fitzpatrick LM, Whiteford JR, King PJ, Bolanos JP, Duchen MR, Waddington SN, and McKay TR.** NRF2 Orchestrates the Metabolic Shift during Induced Pluripotent Stem Cell Reprogramming. *Cell reports* 14: 1883-1891, 2016.
40. **He L, Lee J, Jang JH, Sakchaisri K, Hwang J, Cha-Molstad HJ, Kim KA, Ryoo IJ, Lee HG, Kim SO, Soung NK, Lee KS, Kwon YT, Erikson RL, Ahn JS, and Kim BY.** Osteoporosis regulation by salubrinal through eIF2alpha mediated differentiation of osteoclast and osteoblast. *Cellular signalling* 25: 552-560, 2013.
41. **He Y, Childress P, Hood M, Jr., Alvarez M, Kacena MA, Hanlon M, McKee B, Bidwell JP, and Yang FC.** Nmp4/CIZ suppresses the parathyroid hormone anabolic window by restricting mesenchymal stem cell and osteoprogenitor frequency. *Stem cells and development* 22: 492-500, 2013.
42. **Hopkins A, Mirzayans F, and Berry F.** Foxc1 Expression in Early Osteogenic Differentiation Is Regulated by BMP4-SMAD Activity. *Journal of cellular biochemistry* 117: 1707-1717, 2016.
43. **Huesa C, Yadav MC, Finnila MA, Goodyear SR, Robins SP, Tanner KE, Aspden RM, Millan JL, and Farquharson C.** PHOSPHO1 is essential for mechanically competent mineralization and the avoidance of spontaneous fractures. *Bone* 48: 1066-1074, 2011.
44. **Ishitani T, Ninomiya-Tsuji J, and Matsumoto K.** Regulation of lymphoid enhancer factor 1/T-cell factor by mitogen-activated protein kinase-related Nemo-like kinase-

dependent phosphorylation in Wnt/beta-catenin signaling. *Mol Cell Biol* 23: 1379-1389, 2003.
45. **Ji H, Wu G, Zhan X, Nolan A, Koh C, De Marzo A, Doan HM, Fan J, Cheadle C, Fallahi M, Cleveland JL, Dang CV, and Zeller KI.** Cell-type independent MYC target genes reveal a primordial signature involved in biomass accumulation. *PloS one* 6: e26057, 2011.
46. **Jilka RL.** Inhibiting the inhibitor: a new route to bone anabolism. *Journal of bone and mineral research : the official journal of the American Society for Bone and Mineral Research* 24: 575-577, 2009.
47. **Kalamajski S and Oldberg A.** The role of small leucine-rich proteoglycans in collagen fibrillogenesis. *Matrix biology : journal of the International Society for Matrix Biology* 29: 248-253, 2010.
48. **Karner CM, Esen E, Okunade AL, Patterson BW, and Long F.** Increased glutamine catabolism mediates bone anabolism in response to WNT signaling. *The Journal of clinical investigation* 125: 551-562, 2015.
49. **Karner CM and Long F.** Wnt signaling and cellular metabolism in osteoblasts. *Cellular and molecular life sciences : CMLS* 74: 1649-1657, 2017.
50. **Kress TR, Sabo A, and Amati B.** MYC: connecting selective transcriptional control to global RNA production. *Nature reviews Cancer* 15: 593-607, 2015.
51. **Kristensen LP, Chen L, Nielsen MO, Qanie DW, Kratchmarova I, Kassem M, and Andersen JS.** Temporal profiling and pulsed SILAC labeling identify novel secreted proteins during ex vivo osteoblast differentiation of human stromal stem cells. *Molecular & cellular proteomics : MCP* 11: 989-1007, 2012.
52. **Leder BZ.** Parathyroid Hormone and Parathyroid Hormone-Related Protein Analogs in Osteoporosis Therapy. *Current osteoporosis reports* 15: 110-119, 2017.
53. **Lee WC, Guntur AR, Long F, and Rosen CJ.** Energy Metabolism of the Osteoblast: Implications for Osteoporosis. *Endocrine reviews* 38: 255-266, 2017.
54. **Li J, Yang S, Li X, Liu D, Wang Z, Guo J, Tan N, Gao Z, Zhao X, Zhang J, Gou F, Yokota H, and Zhang P.** Role of endoplasmic reticulum stress in disuse osteoporosis. *Bone* 97: 2-14, 2017.
55. **Li L, Mao J, Sun L, Liu W, and Wu D.** Second cysteine-rich domain of Dickkopf-2 activates canonical Wnt signaling pathway via LRP-6 independently of dishevelled. *The Journal of biological chemistry* 277: 5977-5981, 2002.
56. **Li Q, Gao Z, Chen Y, and Guan MX.** The role of mitochondria in osteogenic, adipogenic and chondrogenic differentiation of mesenchymal stem cells. *Protein & cell* 8: 439-445, 2017.
57. **Li X, Liu P, Liu W, Maye P, Zhang J, Zhang Y, Hurley M, Guo C, Boskey A, Sun L, Harris SE, Rowe DW, Ke HZ, and Wu D.** Dkk2 has a role in terminal osteoblast differentiation and mineralized matrix formation. *Nature genetics* 37: 945-952, 2005.
58. **Liao Y, Smyth GK, and Shi W.** featureCounts: an efficient general purpose program for assigning sequence reads to genomic features. *Bioinformatics* 30: 923-930, 2014.
59. **Lindsay R, Krege JH, Marin F, Jin L, and Stepan JJ.** Teriparatide for osteoporosis: importance of the full course. *Osteoporosis international : a journal established as result of cooperation between the European Foundation for Osteoporosis and the National Osteoporosis Foundation of the USA* 27: 2395-2410, 2016.
60. **Liu X, Bruxvoort KJ, Zylstra CR, Liu J, Cichowski R, Faugere MC, Bouxsein ML, Wan C, Williams BO, and Clemens TL.** Lifelong accumulation of bone in mice lacking Pten in

1150 osteoblasts. *Proceedings of the National Academy of Sciences of the United States of America*
1151 104: 2259-2264, 2007.
1152 61. **Lovato C and Lewiecki EM.** Emerging anabolic agents in the treatment of osteoporosis.
1153 *Expert opinion on emerging drugs*: 1-11, 2017.
1154 62. **Luppen CA, Leclerc N, Noh T, Barski A, Khokhar A, Boskey AL, Smith E, and**
1155 **Frenkel B.** Brief bone morphogenetic protein 2 treatment of glucocorticoid-inhibited
1156 MC3T3-E1 osteoblasts rescues commitment-associated cell cycle and mineralization
1157 without alteration of Runx2. *The Journal of biological chemistry* 278: 44995-45003, 2003.
1158 63. **Ma YL, Bryant HU, Zeng Q, Schmidt A, Hoover J, Cole HW, Yao W, Jee WS, and Sato**
1159 **M.** New bone formation with teriparatide [human parathyroid hormone-(1-34)] is not
1160 retarded by long-term pretreatment with alendronate, estrogen, or raloxifene in
1161 ovariectomized rats. *Endocrinology* 144: 2008-2015, 2003.
1162 64. **Mao B and Niehrs C.** Kremen2 modulates Dickkopf2 activity during Wnt/LRP6
1163 signaling. *Gene* 302: 179-183, 2003.
1164 65. **McBride SH and Silva MJ.** Adaptive and Injury Response of Bone to Mechanical
1165 Loading. *BoneKEy osteovision* 1, 2012.
1166 66. **Meury T, Akhouayri O, Jafarov T, Mandic V, and St-Arnaud R.** Nuclear alpha NAC
1167 influences bone matrix mineralization and osteoblast maturation in vivo. *Mol Cell Biol* 30:
1168 43-53, 2010.
1169 67. **Millan JL.** The role of phosphatases in the initiation of skeletal mineralization. *Calcified*
1170 *tissue international* 93: 299-306, 2013.
1171 68. **Moore DS MG.** *Introduction to the Practice of Statistics*. New York, NY: W.H. Freeman
1172 and Co, 2003.
1173 69. **Morgan S, Poundarik AA, and Vashishth D.** Do Non-collagenous Proteins Affect
1174 Skeletal Mechanical Properties? *Calcified tissue international* 97: 281-291, 2015.
1175 70. **Morinobu M, Nakamoto T, Hino K, Tsuji K, Shen ZJ, Nakashima K, Nifuji A,**
1176 **Yamamoto H, Hirai H, and Noda M.** The nucleocytoplasmic shuttling protein CIZ reduces
1177 adult bone mass by inhibiting bone morphogenetic protein-induced bone formation. *The*
1178 *Journal of experimental medicine* 201: 961-970, 2005.
1179 71. **Morita M, Gravel SP, Hulea L, Larsson O, Pollak M, St-Pierre J, and Topisirovic I.**
1180 mTOR coordinates protein synthesis, mitochondrial activity and proliferation. *Cell cycle*
1181 *(Georgetown, Tex)* 14: 473-480, 2015.
1182 72. **Ng F, Boucher S, Koh S, Sastry KS, Chase L, Lakshmipathy U, Choong C, Yang Z,**
1183 **Vemuri MC, Rao MS, and Tanavde V.** PDGF, TGF-beta, and FGF signaling is important for
1184 differentiation and growth of mesenchymal stem cells (MSCs): transcriptional profiling can
1185 identify markers and signaling pathways important in differentiation of MSCs into
1186 adipogenic, chondrogenic, and osteogenic lineages. *Blood* 112: 295-307, 2008.
1187 73. **Nie Z, Hu G, Wei G, Cui K, Yamane A, Resch W, Wang R, Green DR, Tessarollo L,**
1188 **Casellas R, Zhao K, and Levens D.** c-Myc is a universal amplifier of expressed genes in
1189 lymphocytes and embryonic stem cells. *Cell* 151: 68-79, 2012.
1190 74. **Nifuji A, Ideno H, Ohyama Y, Takanabe R, Araki R, Abe M, Noda M, and Shibuya H.**
1191 Nemo-like kinase (NLK) expression in osteoblastic cells and suppression of osteoblastic
1192 differentiation. *Experimental cell research* 316: 1127-1136, 2010.
1193 75. **Nikel O, Laurencin D, McCallum SA, Gundberg CM, and Vashishth D.** NMR
1194 investigation of the role of osteocalcin and osteopontin at the organic-inorganic interface in
1195 bone. *Langmuir : the ACS journal of surfaces and colloids* 29: 13873-13882, 2013.

76. **Nikitovic D, Aggelidakis J, Young MF, Iozzo RV, Karamanos NK, and Tzanakakis GN.** The biology of small leucine-rich proteoglycans in bone pathophysiology. *The Journal of biological chemistry* 287: 33926-33933, 2012.
77. **Ortega-Molina A and Serrano M.** PTEN in cancer, metabolism, and aging. *Trends in endocrinology and metabolism: TEM* 24: 184-189, 2013.
78. **Owen TA, Aronow M, Shalhoub V, Barone LM, Wilming L, Tassinari MS, Kennedy MB, Pockwinse S, Lian JB, and Stein GS.** Progressive development of the rat osteoblast phenotype in vitro: reciprocal relationships in expression of genes associated with osteoblast proliferation and differentiation during formation of the bone extracellular matrix. *Journal of cellular physiology* 143: 420-430, 1990.
79. **Palomaki S, Pietila M, Laitinen S, Pesala J, Sormunen R, Lehenkari P, and Koivunen P.** HIF-1alpha is upregulated in human mesenchymal stem cells. *Stem cells (Dayton, Ohio)* 31: 1902-1909, 2013.
80. **Pandey AC, Semon JA, Kaushal D, O'Sullivan RP, Glowacki J, Gimble JM, and Bunnell BA.** MicroRNA profiling reveals age-dependent differential expression of nuclear factor kappaB and mitogen-activated protein kinase in adipose and bone marrow-derived human mesenchymal stem cells. *Stem cell research & therapy* 2: 49, 2011.
81. **Pattappa G, Heywood HK, de Bruijn JD, and Lee DA.** The metabolism of human mesenchymal stem cells during proliferation and differentiation. *Journal of cellular physiology* 226: 2562-2570, 2011.
82. **Pellegrini GG, Cregor M, McAndrews K, Morales CC, McCabe LD, McCabe GP, Peacock M, Burr D, Weaver C, and Bellido T.** Nrf2 regulates mass accrual and the antioxidant endogenous response in bone differently depending on the sex and age. *PloS one* 12: e0171161, 2017.
83. **Ponnapakkam T, Katikaneni R, Sakon J, Stratford R, and Gensure RC.** Treating osteoporosis by targeting parathyroid hormone to bone. *Drug discovery today* 19: 204-208, 2014.
84. **Poundarik AA, Diab T, Sroga GE, Ural A, Boskey AL, Gundberg CM, and Vashishth D.** Dilatational band formation in bone. *Proceedings of the National Academy of Sciences of the United States of America* 109: 19178-19183, 2012.
85. **Regan JN, Lim J, Shi Y, Joeng KS, Arbeit JM, Shohet RV, and Long F.** Up-regulation of glycolytic metabolism is required for HIF1alpha-driven bone formation. *Proceedings of the National Academy of Sciences of the United States of America* 111: 8673-8678, 2014.
86. **Riggs BL, Hodgson SF, O'Fallon WM, Chao EY, Wahner HW, Muhs JM, Cedel SL, and Melton LJ, 3rd.** Effect of fluoride treatment on the fracture rate in postmenopausal women with osteoporosis. *The New England journal of medicine* 322: 802-809, 1990.
87. **Rivas A, Vidal RL, and Hetz C.** Targeting the unfolded protein response for disease intervention. *Expert opinion on therapeutic targets* 19: 1203-1218, 2015.
88. **Robinson MD, McCarthy DJ, and Smyth GK.** edgeR: a Bioconductor package for differential expression analysis of digital gene expression data. *Bioinformatics* 26: 139-140, 2010.
89. **Robinson MD and Oshlack A.** A scaling normalization method for differential expression analysis of RNA-seq data. *Genome Biol* 11: R25, 2010.
90. **Robling AG, Childress P, Yu J, Cotte J, Heller A, Philip BK, and Bidwell JP.** Nmp4/CIZ suppresses parathyroid hormone-induced increases in trabecular bone. *Journal of cellular physiology* 219: 734-743, 2009.

91. **Rozpedek W, Markiewicz L, Diehl JA, Pytel D, and Majsterek I.** Unfolded Protein Response and PERK Kinase as a New Therapeutic Target in the Pathogenesis of Alzheimer's Disease. *Current medicinal chemistry* 22: 3169-3184, 2015.
92. **Sanchez-Riera L and Wilson N.** Fragility Fractures & Their Impact on Older People. *Best practice & research Clinical rheumatology* 31: 169-191, 2017.
93. **Schmidt K, Schinke T, Haberland M, Priemel M, Schilling AF, Mueldner C, Rueger JM, Sock E, Wegner M, and Amling M.** The high mobility group transcription factor Sox8 is a negative regulator of osteoblast differentiation. *J Cell Biol* 168: 899-910, 2005.
94. **Shah AD, Shoback D, and Lewiecki EM.** Sclerostin inhibition: a novel therapeutic approach in the treatment of osteoporosis. *International journal of women's health* 7: 565-580, 2015.
95. **Shao Y, Hernandez-Buquer S, Childress P, Stayrook KR, Alvarez MB, Davis H, Plotkin L, He Y, Condon KW, Burr DB, Warden SJ, Robling AG, Yang FC, Wek RC, Allen MR, and Bidwell JP.** Improving Combination Osteoporosis Therapy In a Preclinical Model of Heightened Osteoanabolism. *Endocrinology* 158: 2722-2740, 2017.
96. **Shum LC, White NS, Mills BN, Bentley KL, and Eliseev RA.** Energy Metabolism in Mesenchymal Stem Cells During Osteogenic Differentiation. *Stem cells and development* 25: 114-122, 2016.
97. **Shyh-Chang N and Ng HH.** The metabolic programming of stem cells. *Genes & development* 31: 336-346, 2017.
98. **Silva BC and Bilezikian JP.** Parathyroid hormone: anabolic and catabolic actions on the skeleton. *Current opinion in pharmacology* 22: 41-50, 2015.
99. **Sogaard CH, Mosekilde L, Richards A, and Mosekilde L.** Marked decrease in trabecular bone quality after five years of sodium fluoride therapy--assessed by biomechanical testing of iliac crest bone biopsies in osteoporotic patients. *Bone* 15: 393-399, 1994.
100. **Sroga GE, Karim L, Colon W, and Vashishth D.** Biochemical characterization of major bone-matrix proteins using nanoscale-size bone samples and proteomics methodology. *Molecular & cellular proteomics : MCP* 10: M110 006718, 2011.
101. **Stamos JL and Weis WI.** The beta-catenin destruction complex. *Cold Spring Harb Perspect Biol* 5: a007898, 2013.
102. **Tan Z, Xie N, Banerjee S, Cui H, Fu M, Thannickal VJ, and Liu G.** The monocarboxylate transporter 4 is required for glycolytic reprogramming and inflammatory response in macrophages. *The Journal of biological chemistry* 290: 46-55, 2015.
103. **Teske BF, Baird TD, and Wek RC.** Methods for analyzing eIF2 kinases and translational control in the unfolded protein response. *Methods in enzymology* 490: 333-356, 2011.
104. **Valenzuela V, Martinez G, Duran-Aniotz C, and Hetz C.** Gene therapy to target ER stress in brain diseases. *Brain research* 1648: 561-570, 2016.
105. **Wang X and Proud CG.** The mTOR pathway in the control of protein synthesis. *Physiology (Bethesda, Md)* 21: 362-369, 2006.
106. **Wei J, Shimazu J, Makinistoglu MP, Maurizi A, Kajimura D, Zong H, Takarada T, Lezaki T, Pessin JE, Hinoi E, and Karsenty G.** Glucose Uptake and Runx2 Synergize to Orchestrate Osteoblast Differentiation and Bone Formation. *Cell* 161: 1576-1591, 2015.
107. **Wickham H.** *ggplot2: elegant graphics for data analysis*. New York: Springer-Verlag, 2009.

108. **Wolf E, Lin CY, Eilers M, and Levens DL.** Taming of the beast: shaping Myc-dependent amplification. *Trends in cell biology* 25: 241-248, 2015.
109. **Wu X, Estwick SA, Chen S, Yu M, Ming W, Nebesio TD, Li Y, Yuan J, Kapur R, Ingram D, Yoder MC, and Yang FC.** Neurofibromin plays a critical role in modulating osteoblast differentiation of mesenchymal stem/progenitor cells. *Human molecular genetics* 15: 2837-2845, 2006.
110. **Xi G, Wai C, DeMambro V, Rosen CJ, and Clemmons DR.** IGFBP-2 directly stimulates osteoblast differentiation. *Journal of bone and mineral research : the official journal of the American Society for Bone and Mineral Research* 29: 2427-2438, 2014.
111. **Xiao L, Fei Y, and Hurley MM.** FGF2 crosstalk with Wnt signaling in mediating the anabolic action of PTH on bone formation. *Bone reports* 9: 136-144, 2018.
112. **Yadav MC, Bottini M, Cory E, Bhattacharya K, Kuss P, Narisawa S, Sah RL, Beck L, Fadeel B, Farquharson C, and Millan JL.** Skeletal Mineralization Deficits and Impaired Biogenesis and Function of Chondrocyte-Derived Matrix Vesicles in Phospho1(-/-) and Phospho1/Pi t1 Double-Knockout Mice. *Journal of bone and mineral research : the official journal of the American Society for Bone and Mineral Research* 31: 1275-1286, 2016.
113. **Yadav MC, Simao AM, Narisawa S, Huesa C, McKee MD, Farquharson C, and Millan JL.** Loss of skeletal mineralization by the simultaneous ablation of PHOSPHO1 and alkaline phosphatase function: a unified model of the mechanisms of initiation of skeletal calcification. *Journal of bone and mineral research : the official journal of the American Society for Bone and Mineral Research* 26: 286-297, 2011.
114. **Young SK, Shao Y, Bidwell JP, and Wek RC.** Nuclear Matrix Protein 4 is a Novel Regulator of Ribosome Biogenesis and Controls the Unfolded Protein Response Via Repression of Gadd34 Expression. *The Journal of biological chemistry*, 2016.

SUPPLEMENTAL TABLE MATERIAL:

Loss of *Nmp4* optimizes osteogenic metabolism and secretion to enhance bone quality

Yu Shao[1], Emily Wichern[2], Paul J. Childress[3], Michele Adaway[2], Jagannath Misra[4], Angela Klunk[2], David B. Burr[2], Ronald C. Wek[4], Amber L. Mosley[4], Yunlong Liu[1], Alexander G. Robling[2], Nickolay Brustovetsky[5], James Hamilton[5], Kylie Jacobs[6], Deepak Vashishth[7], Keith R. Stayrook[8], Matthew R. Allen[2, 9], Joseph M. Wallace[3, 10¶] Joseph P Bidwell[1, 2¶]

1. Department of Medical and Molecular Genetics, Indiana University School of Medicine (IUSM), Indianapolis, IN, 46202
2. Department of Anatomy & Cell Biology, Indiana University School of Medicine (IUSM)
3. Department of Orthopaedic Surgery, IUSM
4. Department of Biochemistry & Molecular Biology, IUSM
5. Department of Pharmacology & Toxicology, IUSM
6. Department of Microbiology & Immunology, IUSM
7. Center for Biotechnology & Interdisciplinary Studies (Rm 2213) and Department of Biomedical Engineering, Rensselaer Polytechnic Institute, 110 8th Street, Troy, NY 12180, USA
8. Lilly Research Laboratories, Eli Lilly and Company, Indianapolis, Indiana 46202
9. Roudebush Veterans Administration Medical Center, Indianapolis, IN
10. Department of Biomedical Engineering, Indiana University-Purdue University at Indianapolis, IN, 46202

List of Materials Included: https://figshare.com/s/aef3382cdc7c02151e6f

Supplemental Table S1: ChIP-seq data, located in separate xlsx file

Supplemental Table S2: RNA-seq data, located in separate xlsx file

Supplemental Table S3: Day 3 IPA canonical pathways, located in separate xls file

Supplemental Table S4: Day 7 IPA canonical pathways, located in separate xls file

NOTE: The following are the legends/description for the Supplemental Tables S1-S4.

Supplemental Table S1: ChIP-seq data, located in separate xlsx file GEO accession number GSE112693 for complete ChIP-Seq dataset

Nmp4 occupancy sties in MC3T3-E1 osteoblast-like cells as determined by ChIP-seq analysis (Childress et al., 2015). Peaks are mapped to mouse genome build mm10. **Column A:** gene IDs from Ensembl genes, UCSC genes, etc; **Column B:** gene symbol; **Column C:** strand; **Column D:** chromosome; **Column E:** location of transcription start site (TSS); **Column F:** location of transcription end site (TES); **Column G:** Location of Nmp4 in Zones 1-4. A peak was assigned to a promoter region if it was within -5 to+2 kb from a transcription start site (TSS, Zone 1). The Nmp4 peak was assigned to Zone 2, the intragenic region, if it was located within the range defined by the TSS and the transcription end site, and not within the promoter range of the same gene. To assign a peak to Zone 3, the intergenic region, it had to be -10 000 kb from the TSS and +10 000 kb from the transcription end site, and not within the promoter range of the same gene. Peaks that did not fit any of these definitions were assigned to the classification “other” (Zone 4). A peak could be assigned to multiple functional regions in an area of the genome harboring multiple genes. *Note for Nmp4 gene occupancy we used genes identified in Zones 1 & 2 and listed in Supplemental Table 2.* Column H: Peak_start, the recorded peak start position; Column I: Peak_end: the recorded peak end position; Column J: Peak_position, the middle point position of a peak; Column K: Peak_value, the peak score. This parameter is the measurement of overall (usually average) enrichment for the region.

Supplemental Table S2: RNA-seq data, located in separate xlsx file [GEO accession number GSE112694] Expression of all genes was normalized based on the expression of Gusb (see Materials and Methods). The columns are defined as follows (also see file)

Chr	chromosome
Start	start position of exons
End	end position of exons
Strand	strand
Length	gene length
KO.day3_vs_WT.day3_logFC	log2 fold change
KO.day3_vs_WT.day3_PValue	p value
KO.day3_vs_WT.day3_FDR	false discovery rate
KO.day7_vs_WT.day7_logFC	log2 fold change
KO.day7_vs_WT.day7_PValue	p value
KO.day7_vs_WT.day7_FDR	false discovery rate
WT.day7_vs_WT.day3_logFC	log2 fold change
WT.day7_vs_WT.day3_PValue	p value
WT.day7_vs_WT.day3_FDR	false discovery rate
KO.day7_vs_KO.day3_logFC	log2 fold change
KO.day7_vs_KO.day3_PValue	p value
KO.day7_vs_KO.day3_FDR	false discovery rate
KO-day7/WT-day7_vs_KO-day3/WT-day3_logFC	log2 fold change
KO-day7/WT-day7_vs_KO-day3/WT-day3_PValue	p value
KO-day7/WT-day7_vs_KO-day3/WT-day3_FDR	false discovery rate
*KOD3_5	cpm (counts per million reads)
KOD3_6	cpm (counts per million reads)
KOD3_7	cpm (counts per million reads)
KOD3_8	cpm (counts per million reads)
KOD7_13	cpm (counts per million reads)
KOD7_14	cpm (counts per million reads)
KOD7_15	cpm (counts per million reads)
KOD7_16	cpm (counts per million reads)
WTD3_1b	cpm (counts per million reads)
WTD3_1	cpm (counts per million reads)
WTD3_3	cpm (counts per million reads)
WTD3_4	cpm (counts per million reads)
WTD7_10b	cpm (counts per million reads)
WTD7_10	cpm (counts per million reads)
WTD7_11	cpm (counts per million reads)
WTD7_9	cpm (counts per million reads)
KOD3_5	raw read count
KOD3_6	raw read count
KOD3_7	raw read count
KOD3_8	raw read count
KOD7_13	raw read count
KOD7_14	raw read count
KOD7_15	raw read count
KOD7_16	raw read count
WTD3_1b	raw read count
WTD3_1	raw read count
WTD3_3	raw read count
WTD3_4	raw read count
WTD7_10b	raw read count
WTD7_10	raw read count
WTD7_11	raw read count
WTD7_9	raw read count

*KOD3_5, KOD3_6, KOD3_7; KOD3_8:	4 technical replicates for *Nmp4*$^{-/-}$ Day 3 in culture
KOD7_13, KOD7_14, KOD7_15, KOD7_16:	4 technical replicates for *Nmp4*$^{-/-}$ Day 7 in culture
WTD3_1b, WTD3_1, WTD3_3, WDT3_4:	4 technical replicates for wild type (WT) Day 3 in culture
WTD7_10b, WTD7_10, WTD7_11, WTD7_9:	4 technical replicates for wild type (WT) Day 7 in culture

Supplemental Table S3: Day 3 IPA canonical pathways, located in separate xls file

IPA Canonical pathways perturbed by loss of *Nmp4* in MPSCs harvested at Day 3 in culture. Pathways were identified as significantly sensitive to *Nmp4* status that achieved a value of –log(p-value) ≥1.30.

- Column A: identity of the canonical pathway;
- Column B: –log(p-value);
- Column C: Ratio, the number of genes listed in the dataset over the total number of genes in the pathway.
- Column D z-score of pathway. The activation state of the pathway is predicted to be increased if the z-score is ≥ 2 and attenuated if the z-score ≤ −2. Those pathways listed as #NUM indicate that the z-score algorithm cannot predict whether the pathway activity is increased or decreased in the *Nmp4*$^{-/-}$ cells.
- Column E: molecules in the dataset belonging to pathway.

Supplemental Table S4: Day 7 IPA canonical pathways, located in separate xls file

IPA Canonical pathways perturbed by loss of *Nmp4* in MPSCs harvested at Day 7 in culture. Pathways were identified as significantly sensitive to *Nmp4* status that achieved a value of –log(p-value) ≥1.30. See **Supplemental Table S3** legend for identity of table columns.

A. Initial mineralization (post-seeding of WT & *Nmp4*$^{-/-}$ MSPCs

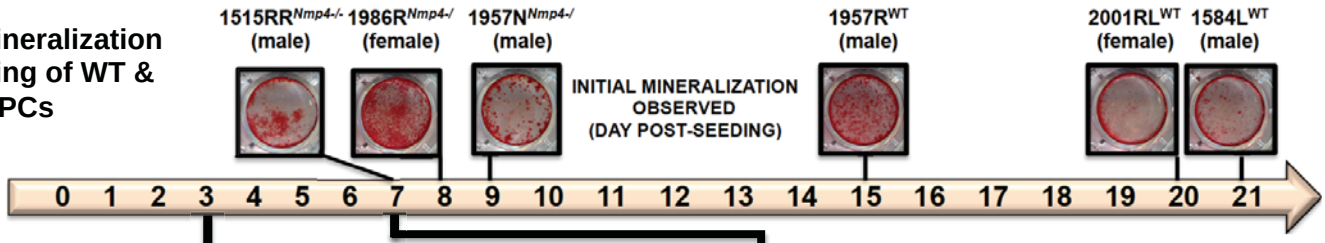

B. Volcano plots Day 3 & Day 7 in culture (RNA-seq)

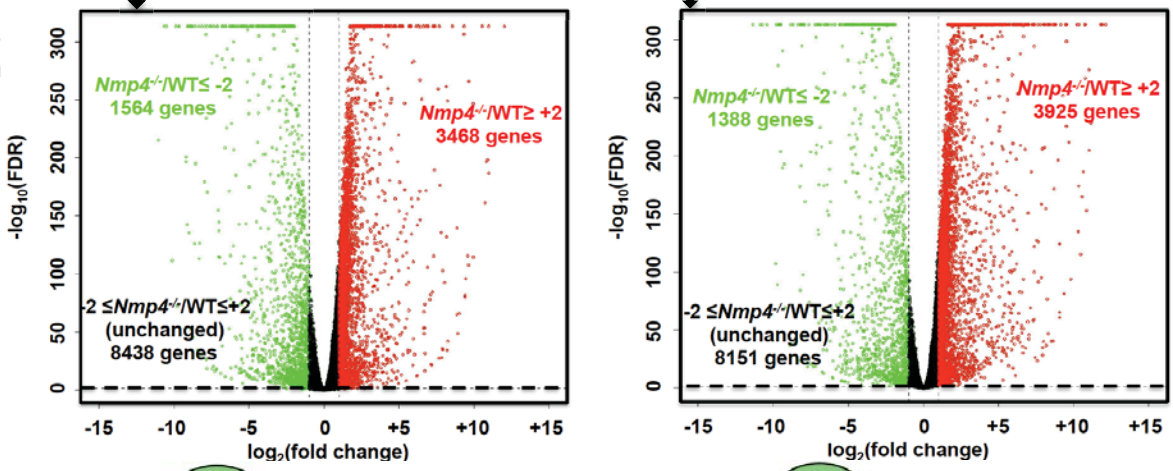

C. Venn diagrams Day 3 & Day 7 ChIP-seq vs RNA-seq

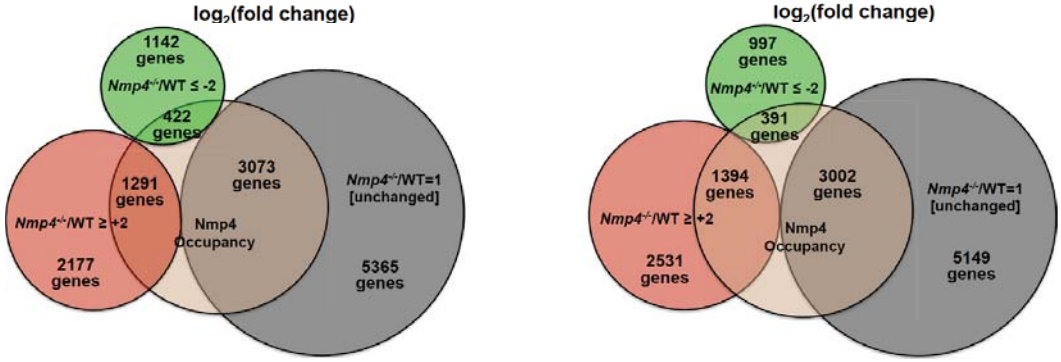

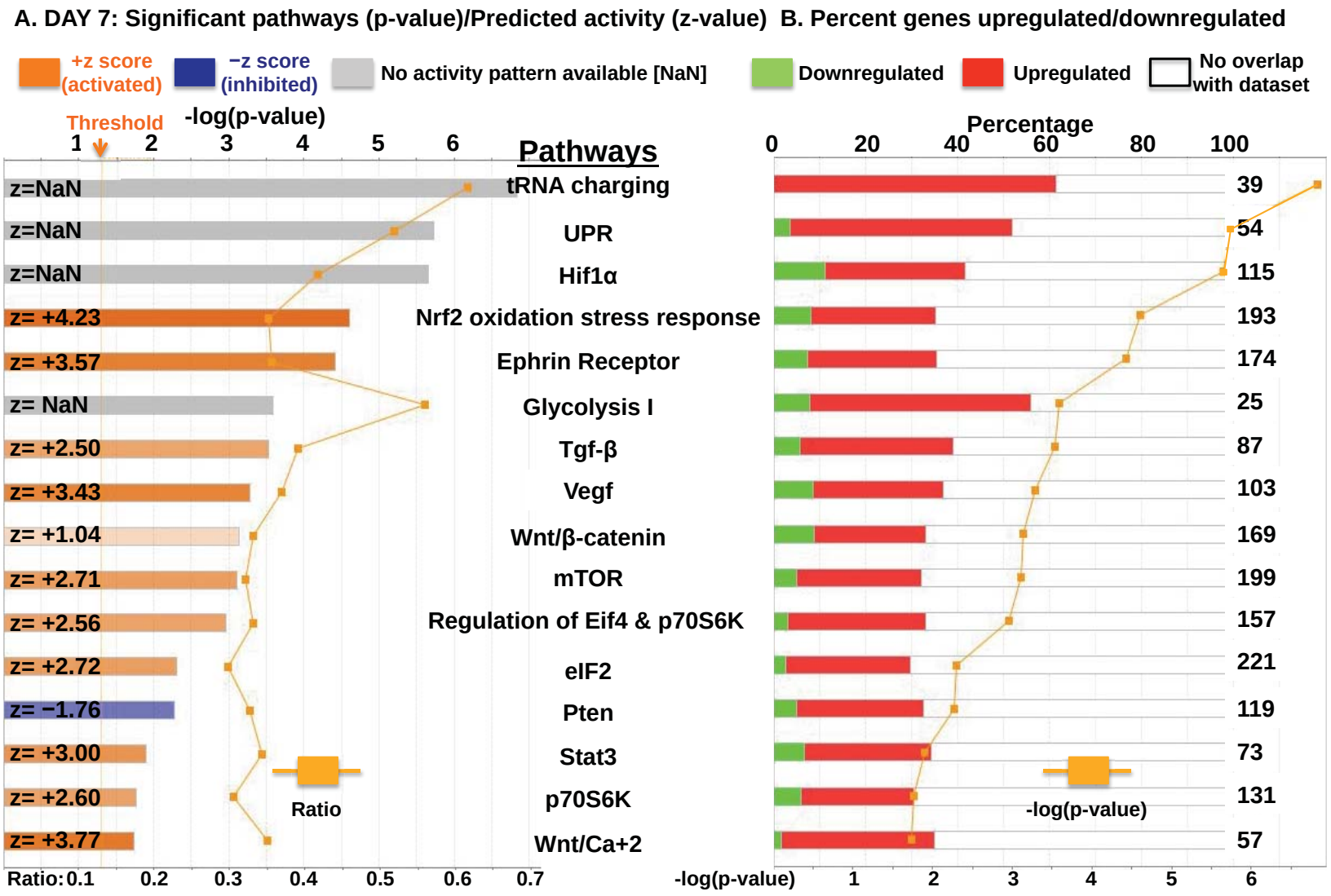
A. DAY 7: Significant pathways (p-value)/Predicted activity (z-value)
B. Percent genes upregulated/downregulated
+z score (activated)
−z score (inhibited)
No activity pattern available [NaN]
Downregulated
Upregulated
No overlap with dataset
Threshold
-log(p-value)
1 2 3 4 5 6
Pathways
Percentage
0 20 40 60 80 100
z=NaN tRNA charging 39
z=NaN UPR 54
z=NaN Hif1α 115
z= +4.23 Nrf2 oxidation stress response 193
z= +3.57 Ephrin Receptor 174
z= NaN Glycolysis I 25
z= +2.50 Tgf-β 87
z= +3.43 Vegf 103
z= +1.04 Wnt/β-catenin 169
z= +2.71 mTOR 199
z= +2.56 Regulation of Eif4 & p70S6K 157
z= +2.72 eIF2 221
z= −1.76 Pten 119
z= +3.00 Stat3 73
z= +2.60 p70S6K 131
z= +3.77 Wnt/Ca+2 57
Ratio
-log(p-value)
Ratio: 0.1 0.2 0.3 0.4 0.5 0.6 0.7
-log(p-value) 1 2 3 4 5 6

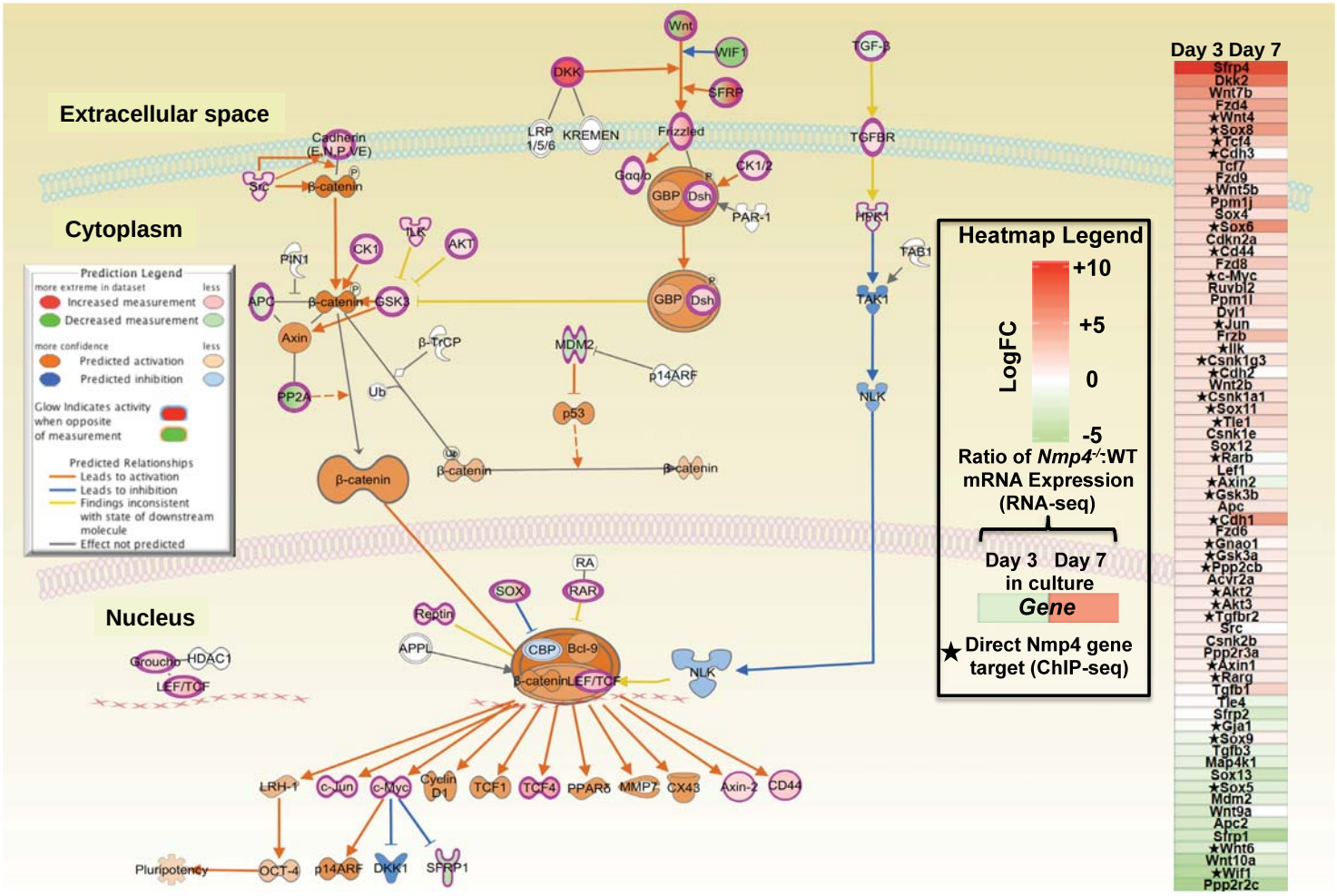
Extracellular space
Cytoplasm
Nucleus
Wnt
WIF1
DKK
SFRP
LRP 1/5/6
KREMEN
Frizzled
Cadherin (E,N,P,VE)
Src
β-catenin
Gαq/o
GBP
Dsh
CK1/2
PAR-1
CK1
ILK
AKT
PIN1
APC
GSK3
Axin
β-TrCP
Ub
PP2A
MDM2
p14ARF
p53
TGF-β
TGFBR
HPK1
TAB1
TAK1
NLK
RA
SOX
RAR
Reptin
APPL
CBP
Bcl-9
LEF/TCF
Groucho
HDAC1
LRH-1
c-Jun
c-Myc
Cyclin D1
TCF1
TCF4
PPARδ
MMP7
CX43
Axin-2
CD44
Pluripotency
OCT-4
p14ARF
DKK1
SFRP1
Prediction Legend
more extreme in dataset
less
Increased measurement
Decreased measurement
more confidence
less
Predicted activation
Predicted inhibition
Glow Indicates activity when opposite of measurement
Predicted Relationships
Leads to activation
Leads to inhibition
Findings inconsistent with state of downstream molecule
Effect not predicted
Heatmap Legend
LogFC
+10
+5
0
-5
Ratio of Nmp4-/-:WT mRNA Expression (RNA-seq)
Day 3 Day 7 in culture
Gene
★ Direct Nmp4 gene target (ChIP-seq)
Day 3 Day 7
Sfrp4
Dkk2
Wnt7b
Fzd4
★Wnt4
★Sox8
★Tcf4
★Cdh3
Tcf7
Fzd9
★Wnt5b
Ppm1j
Sox4
★Sox6
Cdkn2a
★Cd44
Fzd8
★c-Myc
Ruvbl2
Ppm1l
Dyl1
★Jun
Frzb
★Ilk
★Csnk1g3
★Cdh2
Wnt2b
★Csnk1a1
★Sox11
★Tle1
Csnk1e
Sox12
★Rarb
Lef1
★Axin2
★Gsk3b
Apc
★Cdh1
Fzd6
★Gnaq1
★Gsk3a
★Ppp2cb
Acvr2a
★Akt2
★Akt3
★Tgfbr2
Src
Csnk2b
Ppp2r3a
★Axin1
★Rarg
Tgfb1
Tle4
Sfrp2
★Gja1
★Sox9
Tgfb3
Map4k1
Sox13
★Sox5
Mdm2
Wnt9a
Apc2
Sfrp1
★Wnt6
Wnt10a
★Wif1
Ppp2r2c

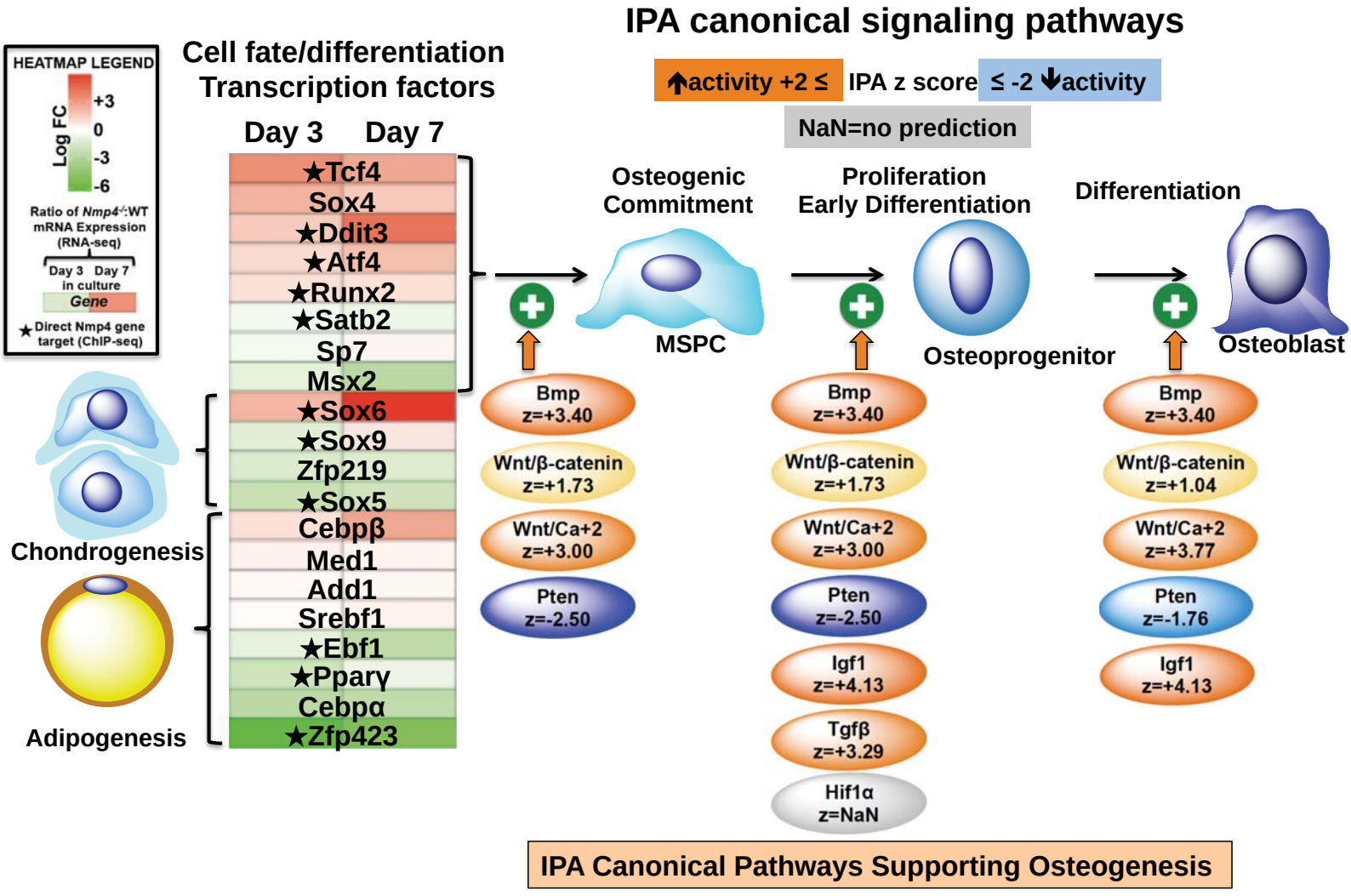
HEATMAP LEGEND
Log FC
+3
0
-3
-6
Ratio of Nmp4-/-:WT mRNA Expression (RNA-seq)
Day 3 Day 7 in culture
Gene
★Direct Nmp4 gene target (ChIP-seq)
Cell fate/differentiation Transcription factors
Day 3 Day 7
★Tcf4
Sox4
★Ddit3
★Atf4
★Runx2
★Satb2
Sp7
Msx2
★Sox6
★Sox9
Zfp219
★Sox5
Cebpβ
Med1
Add1
Srebf1
★Ebf1
★Pparγ
Cebpα
★Zfp423
Chondrogenesis
Adipogenesis
IPA canonical signaling pathways
activity +2 ≤
IPA z score
≤ -2 activity
NaN=no prediction
Osteogenic Commitment
Proliferation Early Differentiation
Differentiation
MSPC
Osteoprogenitor
Osteoblast
Bmp z=+3.40
Wnt/β-catenin z=+1.73
Wnt/Ca+2 z=+3.00
Pten z=-2.50
Igf1 z=+4.13
Tgfβ z=+3.29
Hif1α z=NaN
Bmp z=+3.40
Wnt/β-catenin z=+1.04
Wnt/Ca+2 z=+3.77
Pten z=-1.76
Igf1 z=+4.13
IPA Canonical Pathways Supporting Osteogenesis

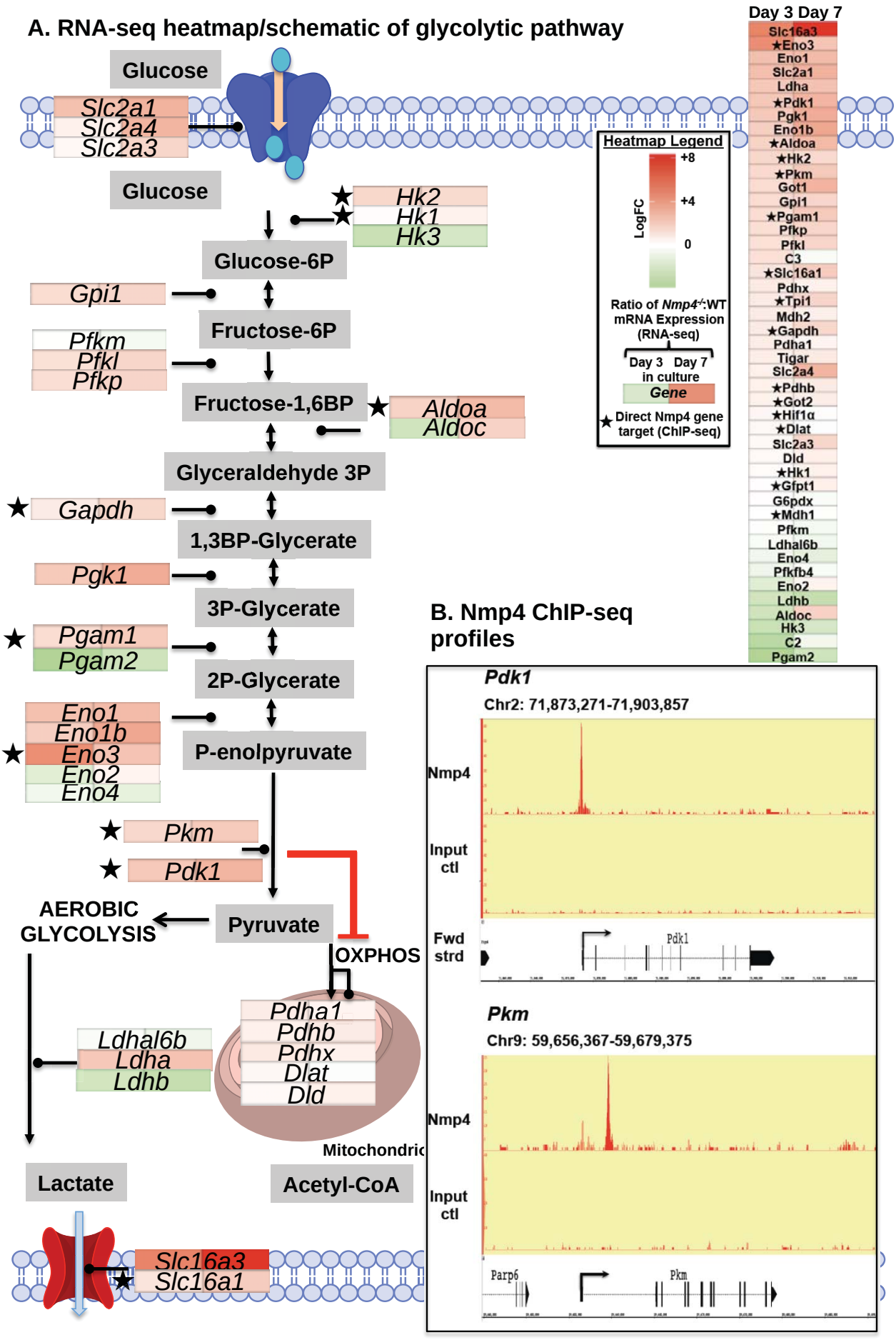
A. RNA-seq heatmap/schematic of glycolytic pathway
Day 3 Day 7
Slc16a3
★Eno3
Eno1
Slc2a1
Ldha
★Pdk1
Pgk1
Eno1b
★Aldoa
★Hk2
★Pkm
Got1
Gpi1
★Pgam1
Pfkp
Pfkl
C3
★Slc16a1
Pdhx
★Tpi1
Mdh2
★Gapdh
Pdha1
Tigar
Slc2a4
★Pdhb
★Got2
★Hif1α
★Dlat
Slc2a3
Dld
★Hk1
★Gfpt1
G6pdx
★Mdh1
Pfkm
Ldhal6b
Eno4
Pfkfb4
Eno2
Ldhb
Aldoc
Hk3
C2
Pgam2
Heatmap Legend
LogFC
+8
+4
0
Ratio of Nmp4-/-:WT mRNA Expression (RNA-seq)
Day 3 Day 7 in culture
Gene
★ Direct Nmp4 gene target (ChIP-seq)
Glucose
Slc2a1
Slc2a4
Slc2a3
Glucose
★ Hk2
★ Hk1
Hk3
Glucose-6P
Gpi1
Fructose-6P
Pfkm
Pfkl
Pfkp
Fructose-1,6BP
★ Aldoa
Aldoc
Glyceraldehyde 3P
★ Gapdh
1,3BP-Glycerate
Pgk1
3P-Glycerate
★ Pgam1
Pgam2
2P-Glycerate
Eno1
Eno1b
★ Eno3
Eno2
Eno4
P-enolpyruvate
★ Pkm
★ Pdk1
AEROBIC GLYCOLYSIS
Pyruvate
OXPHOS
Pdha1
Pdhb
Pdhx
Dlat
Dld
Ldhal6b
Ldha
Ldhb
Mitochondric
Lactate
Acetyl-CoA
Slc16a3
★ Slc16a1
B. Nmp4 ChIP-seq profiles
Pdk1
Chr2: 71,873,271-71,903,857
Nmp4
Input ctl
Fwd strd
Pdk1
Pkm
Chr9: 59,656,367-59,679,375
Nmp4
Input ctl
Parp6
Pkm

A Glycolytic stress test for 1957N^{KO} vs. 1957R^{WT}

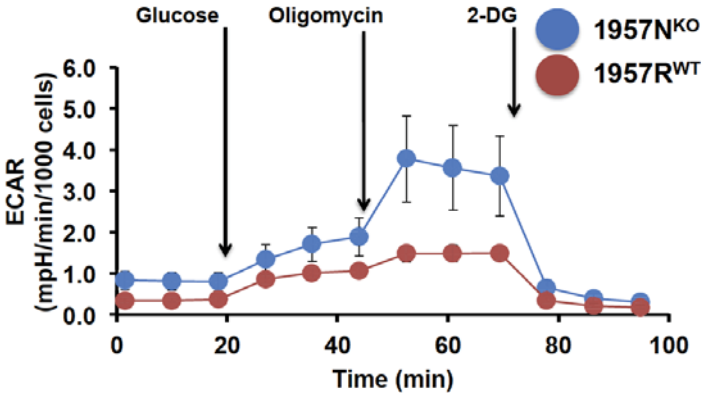

B Glycolytic stress test for 1515RR^{KO} vs.1584L^{WT}

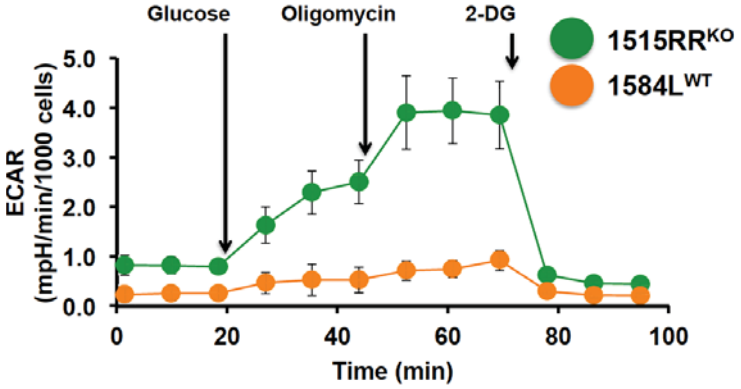

C Statistical analysis of combined data

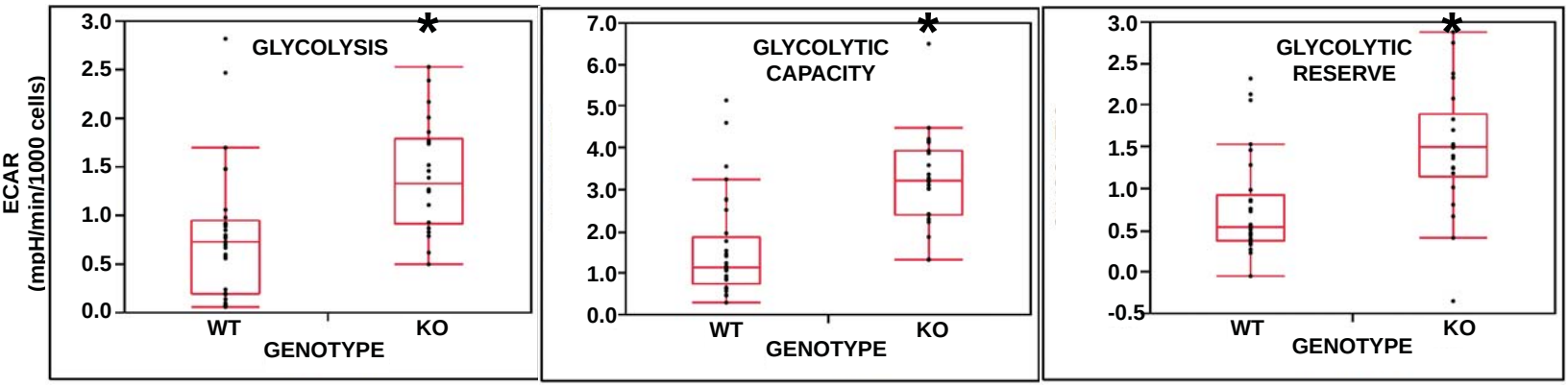

A Mito stress test for 1957N^{KO} vs. 1957R^{WT}

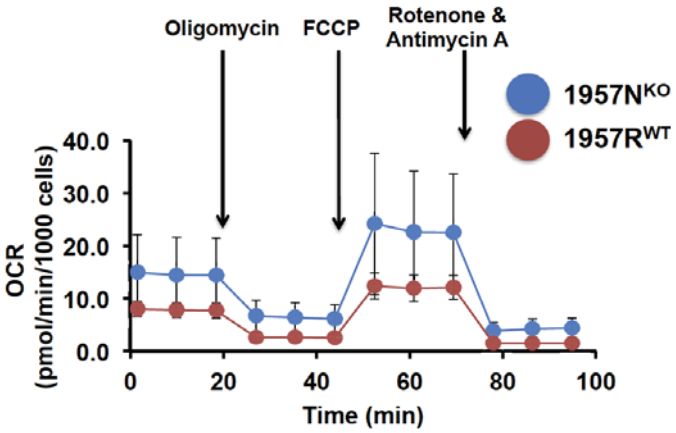

B Mito stress test for 1515RR^{KO} vs.1584L^{WT}

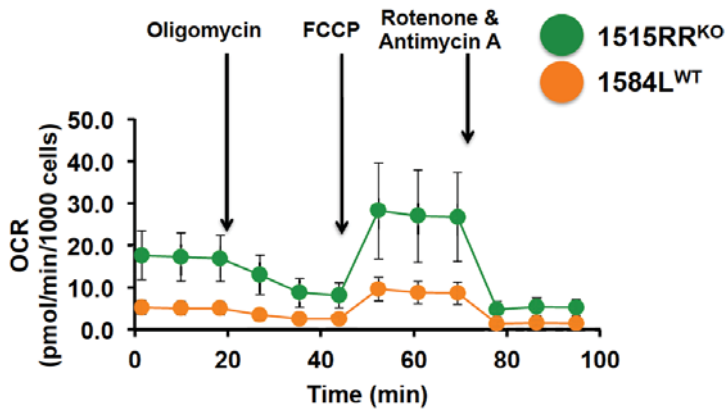

C Statistical analysis of combined data

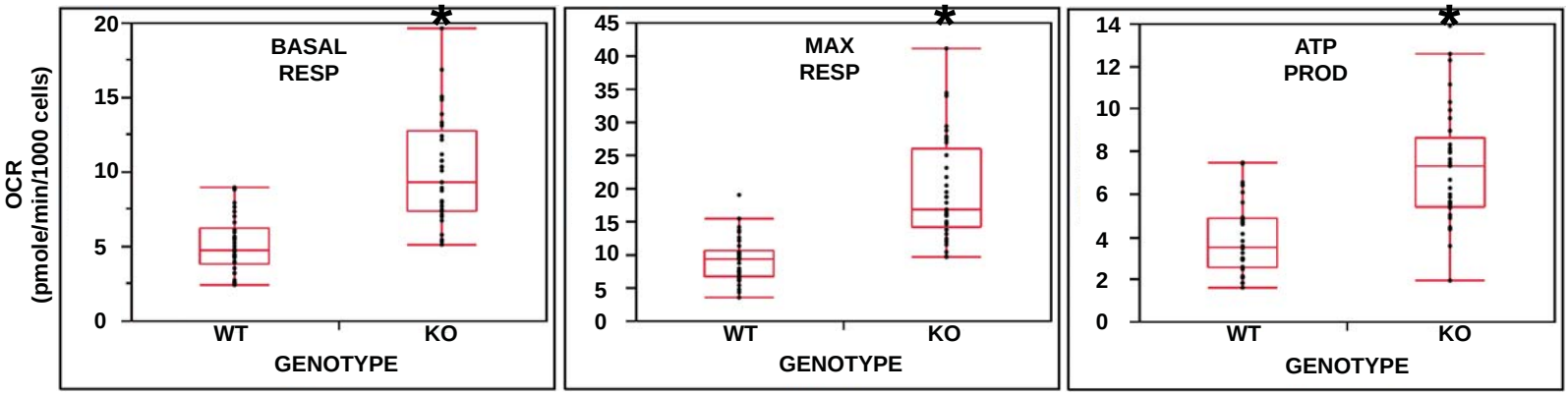

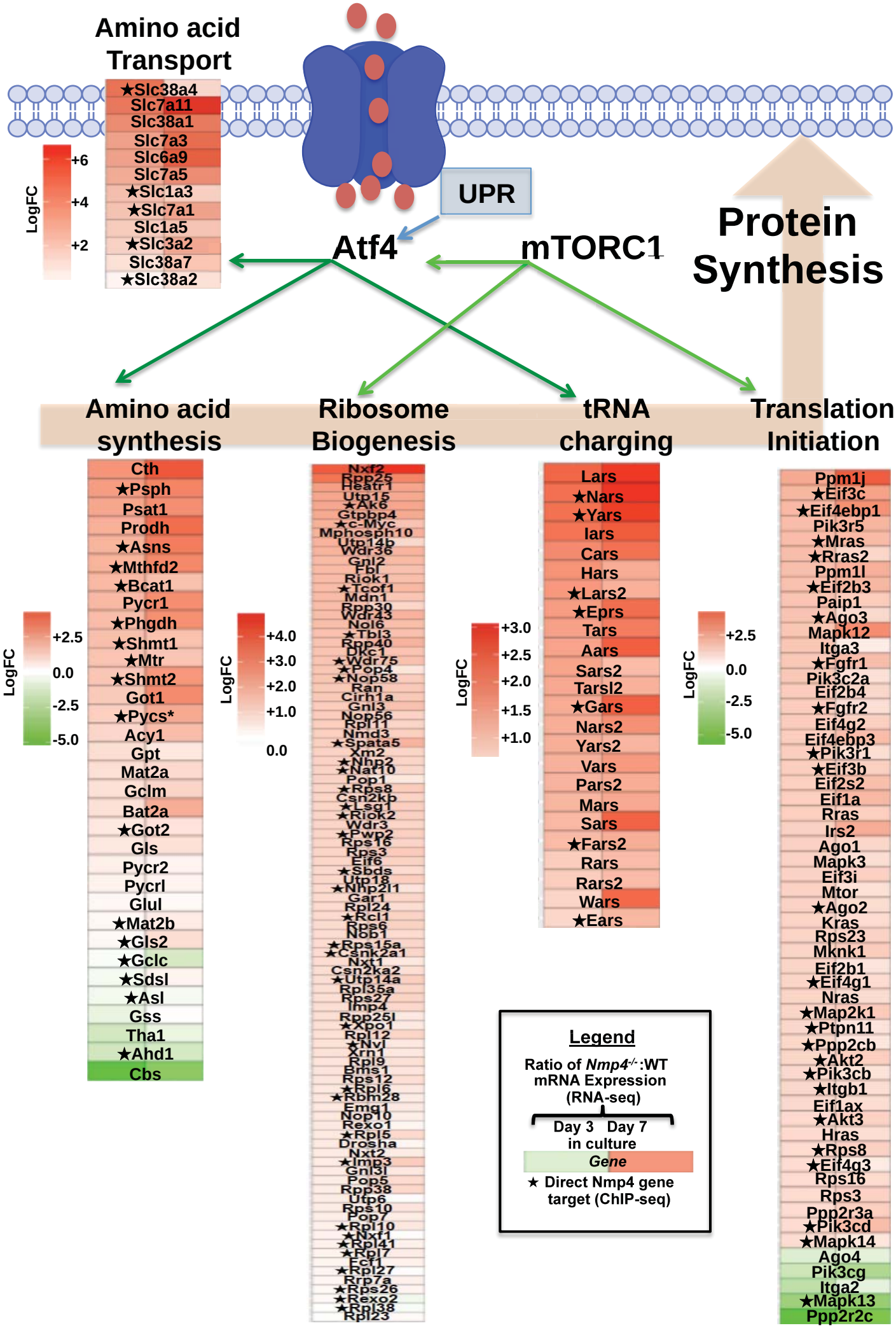
Amino acid Transport
★Slc38a4
Slc7a11
Slc38a1
Slc7a3
Slc6a9
Slc7a5
★Slc1a3
★Slc7a1
Slc1a5
★Slc3a2
Slc38a7
★Slc38a2
LogFC
+6
+4
+2
UPR
Atf4
mTORC1
Protein Synthesis
Amino acid synthesis
Ribosome Biogenesis
tRNA charging
Translation Initiation
Cth
★Psph
Psat1
Prodh
★Asns
★Mthfd2
★Bcat1
Pycr1
★Phgdh
★Shmt1
★Mtr
★Shmt2
Got1
★Pycs*
Acy1
Gpt
Mat2a
Gclm
Bat2a
★Got2
Gls
Pycr2
Pycrl
Glul
★Mat2b
★Gls2
★Gclc
★Sdsl
★Asl
Gss
Tha1
★Ahd1
Cbs
LogFC
+2.5
0.0
-2.5
-5.0
Nxf2
Rpp25
Heatr1
Utp15
★Ak6
Gtpbp4
★c-Myc
Mphosph10
Utp14b
Wdr36
Gnl2
Fbl
Riok1
★Tcof1
Mdn1
Rpp30
Wdr43
Nol6
★Tbl3
Rpp40
Dkc1
★Wdr75
★Pop4
★Nop58
Ran
Cirh1a
Gnl3
Nop56
Rpl11
Nmd3
★Spata5
Xrn2
★Nhp2
★Nat10
Pop1
★Rps8
Csn2kb
★Lsg1
★Riok2
Wdr3
★Pwp2
Rps16
Rps3
Eif6
★Sbds
Utp18
★Nhp2l1
Gar1
Rpl24
★Rcl1
Rps6
Nob1
★Rps15a
★Csnk2a1
Nxt1
Csn2ka2
★Utp14a
Rpl35a
Rps27
Imp4
Rpp25l
★Xpo1
Rpl12
★Nvl
Xrn1
Rpl9
Bms1
Rps12
★Rpl6
★Rbm28
Emg1
Nop10
Rexo1
★Rpl5
Drosha
Nxt2
★Imp3
Gnl3l
Pop5
Rpp38
Utp6
Rps10
Pop7
★Rpl10
★Nxf1
★Rpl41
★Rpl7
Fcf1
★Rpl27
Rrp7a
★Rps26
★Rexo2
★Rpl38
Rpl23
LogFC
+4.0
+3.0
+2.0
+1.0
0.0
Lars
★Nars
★Yars
Iars
Cars
Hars
★Lars2
★Eprs
Tars
Aars
Sars2
Tarsl2
★Gars
Nars2
Yars2
Vars
Pars2
Mars
Sars
★Fars2
Rars
Rars2
Wars
★Ears
LogFC
+3.0
+2.5
+2.0
+1.5
+1.0
Ppm1j
★Eif3c
★Eif4ebp1
Pik3r5
★Mras
★Rras2
Ppm1l
★Eif2b3
Paip1
★Ago3
Mapk12
Itga3
★Fgfr1
Pik3c2a
Eif2b4
★Fgfr2
Eif4g2
Eif4ebp3
★Pik3r1
★Eif3b
Eif2s2
Eif1a
Rras
Irs2
Ago1
Mapk3
Eif3i
Mtor
★Ago2
Kras
Rps23
Mknk1
Eif2b1
★Eif4g1
Nras
★Map2k1
★Ptpn11
★Ppp2cb
★Akt2
★Pik3cb
★Itgb1
Eif1ax
★Akt3
Hras
★Rps8
★Eif4g3
Rps16
Rps3
Ppp2r3a
★Pik3cd
★Mapk14
Ago4
Pik3cg
Itga2
★Mapk13
Ppp2r2c
LogFC
+2.5
0.0
-2.5
-5.0
Legend
Ratio of Nmp4-/-:WT mRNA Expression (RNA-seq)
Day 3 Day 7 in culture
Gene
★ Direct Nmp4 gene target (ChIP-seq)

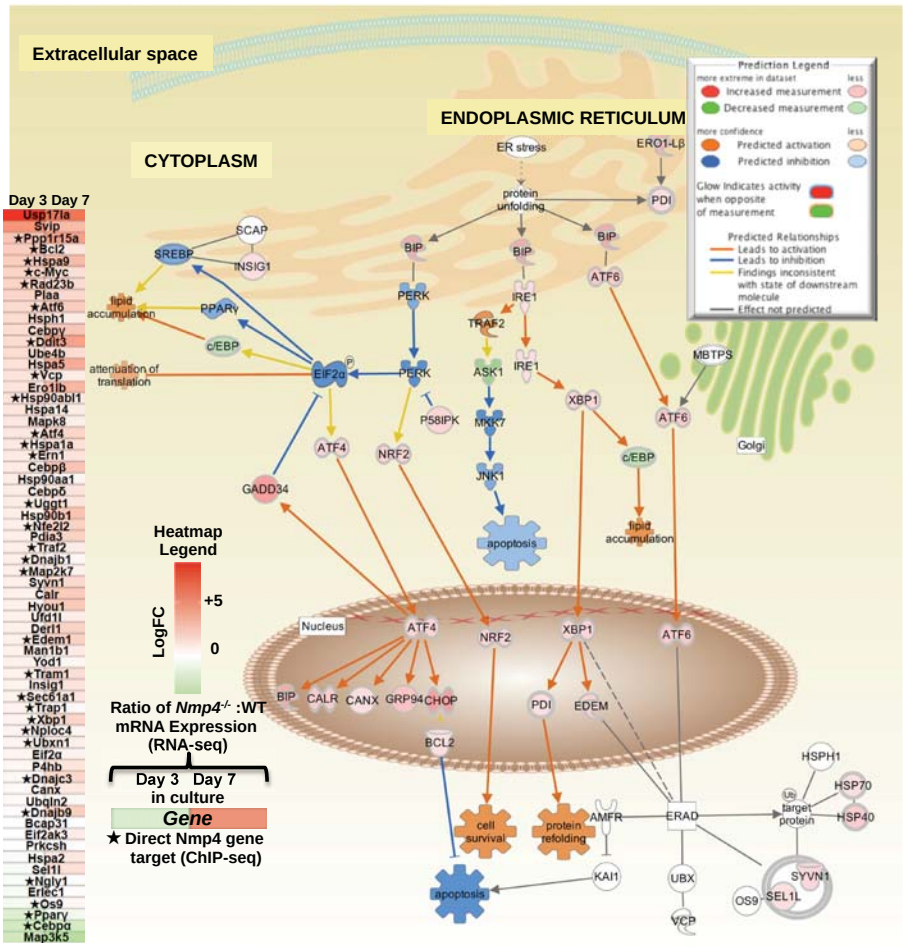
Extracellular space
CYTOPLASM
ENDOPLASMIC RETICULUM
Golgi
Nucleus
Day 3 Day 7
Usp17la
Svip
★Ppp1r15a
★Bcl2
★Hspa9
★c-Myc
★Rad23b
Plaa
★Atf6
Hsph1
Cebpγ
★Ddit3
Ube4b
Hspa5
★Vcp
Ero1lb
★Hsp90abl1
Hspa14
Mapk8
★Atf4
★Hspa1a
★Ern1
Cebpβ
Hsp90aa1
Cebpδ
★Uggt1
Hsp90b1
★Nfe2l2
Pdia3
★Traf2
★Dnajb1
★Map2k7
Syvn1
Calr
Hyou1
Ufd1l
Derl1
★Edem1
Man1b1
Yod1
★Tram1
Insig1
★Sec61a1
★Trap1
★Xbp1
★Nploc4
★Ubxn1
Eif2α
P4hb
★Dnajc3
Canx
Ubqln2
★Dnajb9
Bcap31
Eif2ak3
Prkcsh
Hspa2
Sel1l
★Ngly1
Erlec1
★Os9
★Pparγ
★Cebpα
Map3k5
Heatmap Legend
LogFC
+5
0
Ratio of Nmp4-/- :WT mRNA Expression (RNA-seq)
Day 3 Day 7 in culture
Gene
★ Direct Nmp4 gene target (ChIP-seq)
Prediction Legend
more extreme in dataset
less
Increased measurement
Decreased measurement
more confidence
less
Predicted activation
Predicted inhibition
Glow Indicates activity when opposite of measurement
Predicted Relationships
Leads to activation
Leads to inhibition
Findings inconsistent with state of downstream molecule
Effect not predicted
ER stress
ERO1-Lβ
protein unfolding
PDI
BIP
SCAP
SREBP
INSIG1
PERK
IRE1
ATF6
TRAF2
ASK1
MBTPS
lipid accumulation
PPARγ
c/EBP
attenuation of translation
EIF2α
P58IPK
XBP1
MKK7
ATF4
NRF2
JNK1
GADD34
apoptosis
BIP
CALR
CANX
GRP94
CHOP
PDI
EDEM
BCL2
HSPH1
HSP70
HSP40
target protein
cell survival
protein refolding
AMFR
ERAD
KAI1
UBX
SYVN1
OS9
SEL1L
VCP

WT
Nmp4$^{-/-}$

A. Total polyribosome profiling of MSPCs

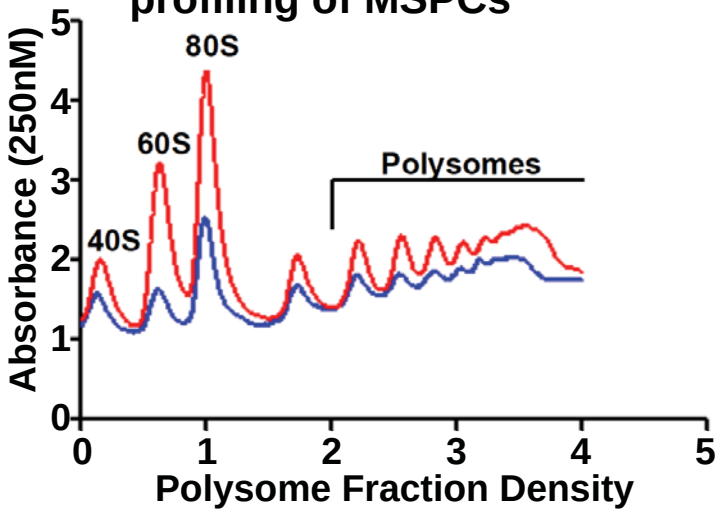

B. *Col1a1* mRNA expression

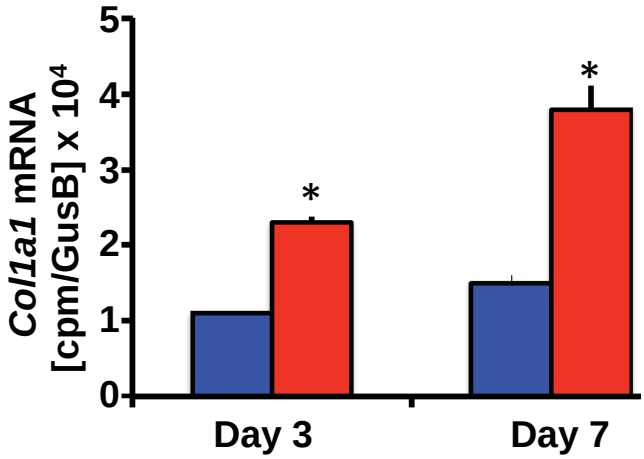

C. *Col1a1* mRNA association with MSPC polyribosome [Day 4]

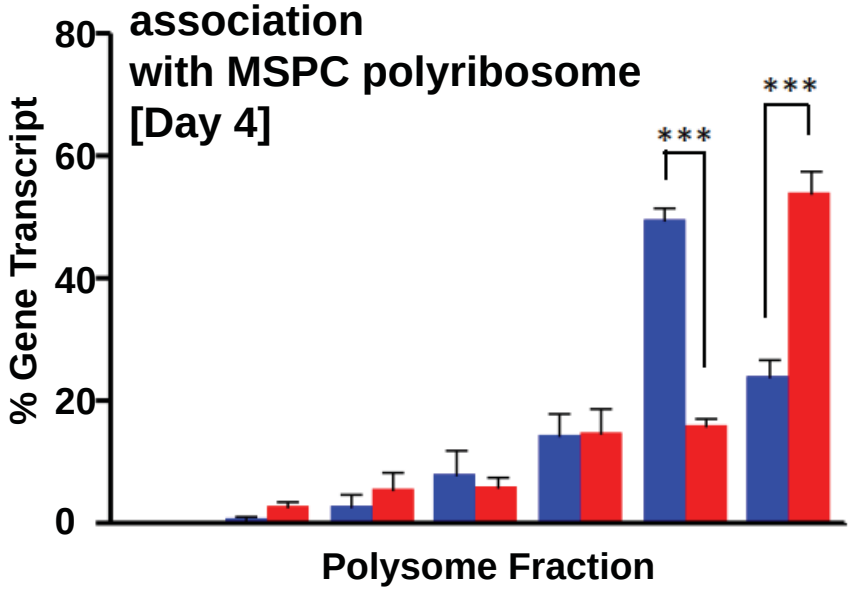

D. MSPC collagen protein secretion

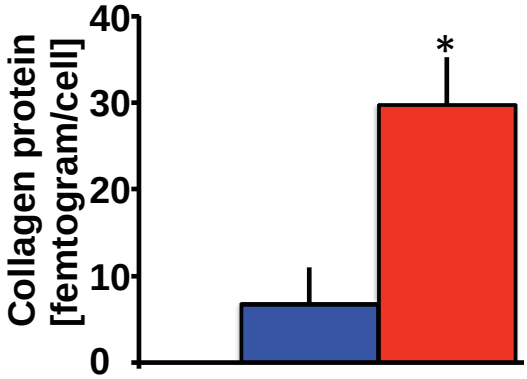

E. MSPC collagen secretion and proliferation activity

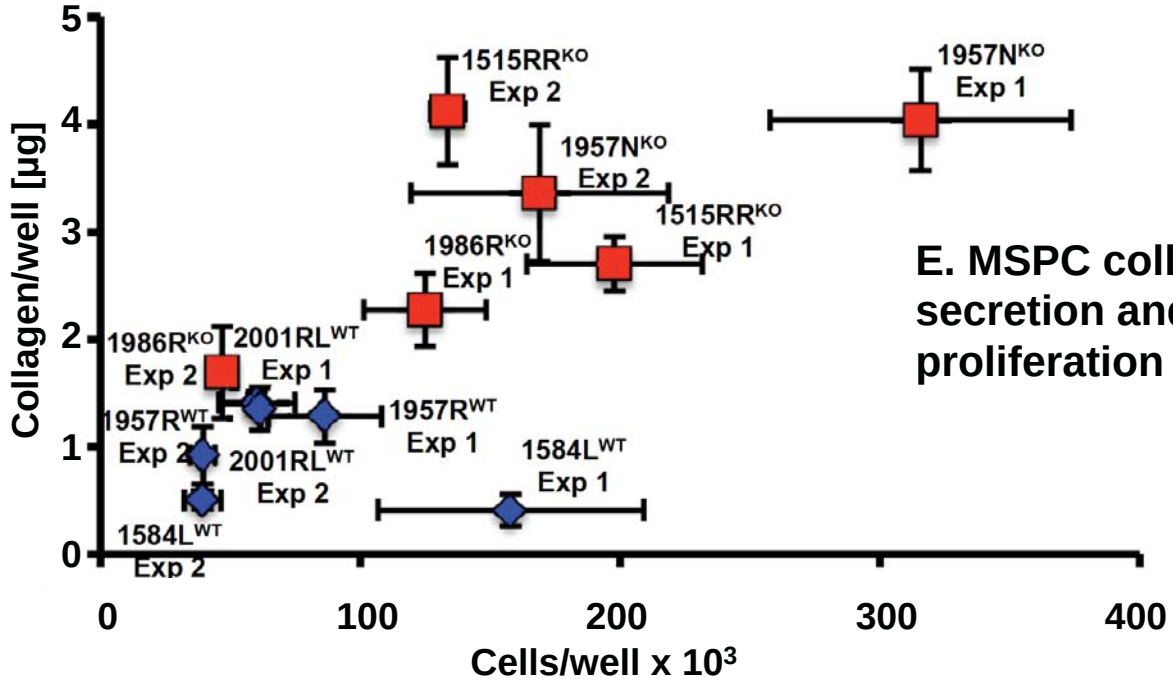

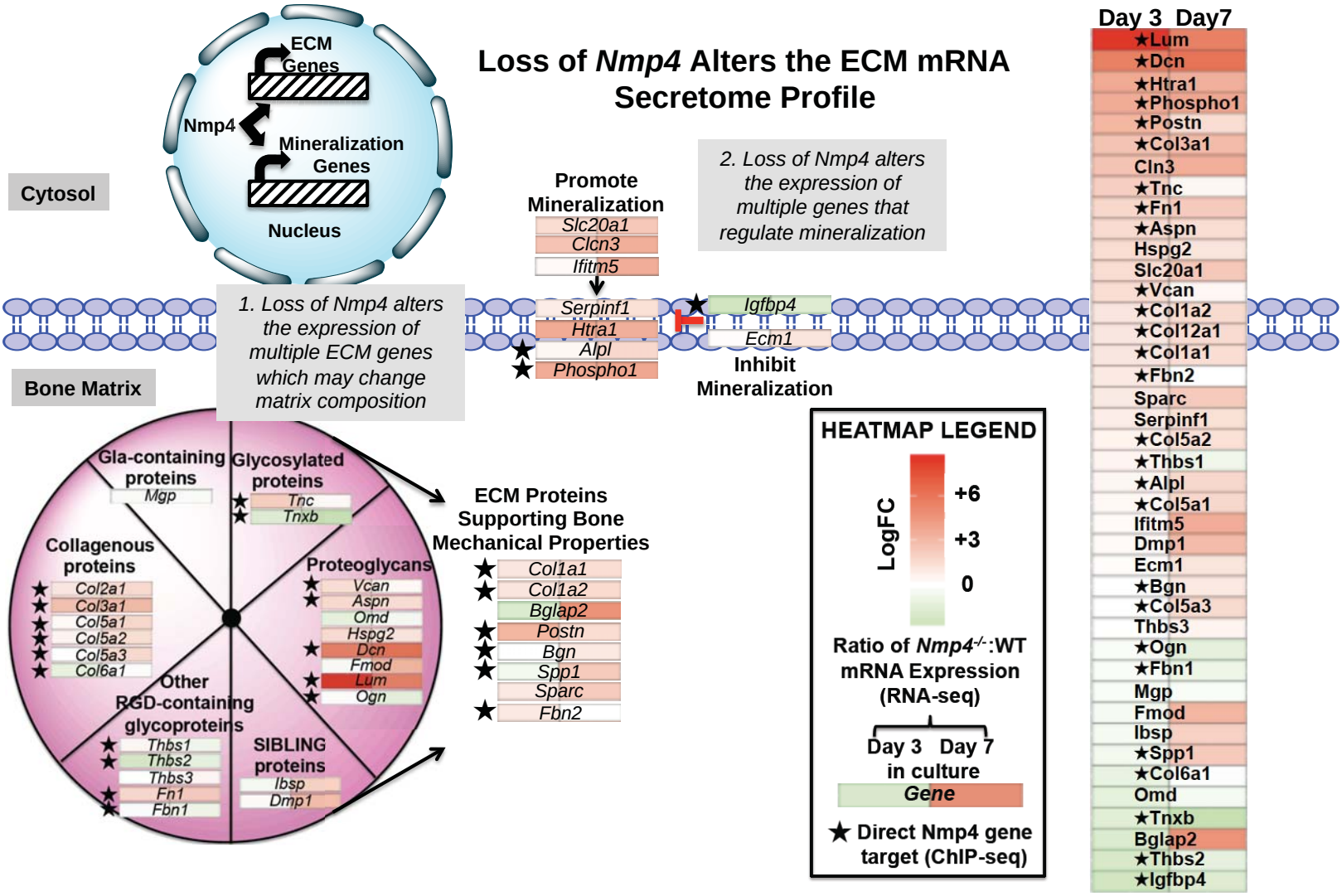
Loss of Nmp4 Alters the ECM mRNA Secretome Profile
ECM Genes
Nmp4
Mineralization Genes
Nucleus
Cytosol
Bone Matrix
1. Loss of Nmp4 alters the expression of multiple ECM genes which may change matrix composition
2. Loss of Nmp4 alters the expression of multiple genes that regulate mineralization
Promote Mineralization
Slc20a1
Clcn3
Ifitm5
Serpinf1
Htra1
Alpl
Phospho1
Igfbp4
Ecm1
Inhibit Mineralization
Gla-containing proteins
Mgp
Glycosylated proteins
Tnc
Tnxb
Collagenous proteins
Col2a1
Col3a1
Col5a1
Col5a2
Col5a3
Col6a1
Proteoglycans
Vcan
Aspn
Omd
Hspg2
Dcn
Fmod
Lum
Ogn
Other RGD-containing glycoproteins
Thbs1
Thbs2
Thbs3
Fn1
Fbn1
SIBLING proteins
Ibsp
Dmp1
ECM Proteins Supporting Bone Mechanical Properties
Col1a1
Col1a2
Bglap2
Postn
Bgn
Spp1
Sparc
Fbn2
HEATMAP LEGEND
LogFC
+6
+3
0
Ratio of Nmp4-/-:WT mRNA Expression (RNA-seq)
Day 3 Day 7 in culture
Gene
Direct Nmp4 gene target (ChIP-seq)
Day 3 Day7
Lum
Dcn
Htra1
Phospho1
Postn
Col3a1
Cln3
Tnc
Fn1
Aspn
Hspg2
Slc20a1
Vcan
Col1a2
Col12a1
Col1a1
Fbn2
Sparc
Serpinf1
Col5a2
Thbs1
Alpl
Col5a1
Ifitm5
Dmp1
Ecm1
Bgn
Col5a3
Thbs3
Ogn
Fbn1
Mgp
Fmod
Ibsp
Spp1
Col6a1
Omd
Tnxb
Bglap2
Thbs2
Igfbp4

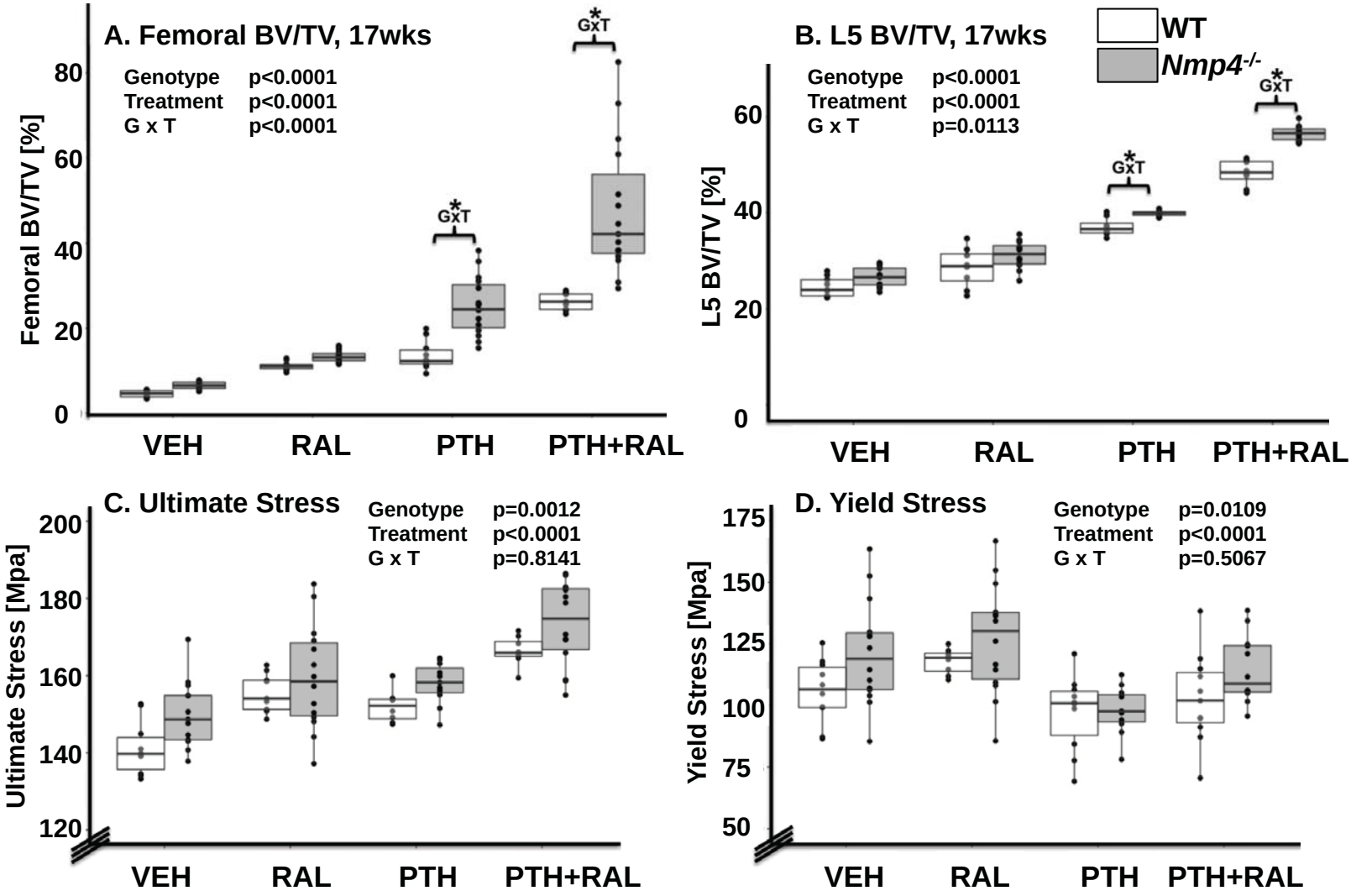
A. Femoral BV/TV, 17wks
Genotype p<0.0001
Treatment p<0.0001
G x T p<0.0001
Femoral BV/TV [%]
0
20
40
60
80
G x T
VEH
RAL
PTH
PTH+RAL
B. L5 BV/TV, 17wks
WT
Nmp4-/-
Genotype p<0.0001
Treatment p<0.0001
G x T p=0.0113
L5 BV/TV [%]
0
20
40
60
G x T
VEH
RAL
PTH
PTH+RAL
C. Ultimate Stress
Genotype p=0.0012
Treatment p<0.0001
G x T p=0.8141
Ultimate Stress [Mpa]
120
140
160
180
200
VEH
RAL
PTH
PTH+RAL
D. Yield Stress
Genotype p=0.0109
Treatment p<0.0001
G x T p=0.5067
Yield Stress [Mpa]
50
75
100
125
150
175
VEH
RAL
PTH
PTH+RAL

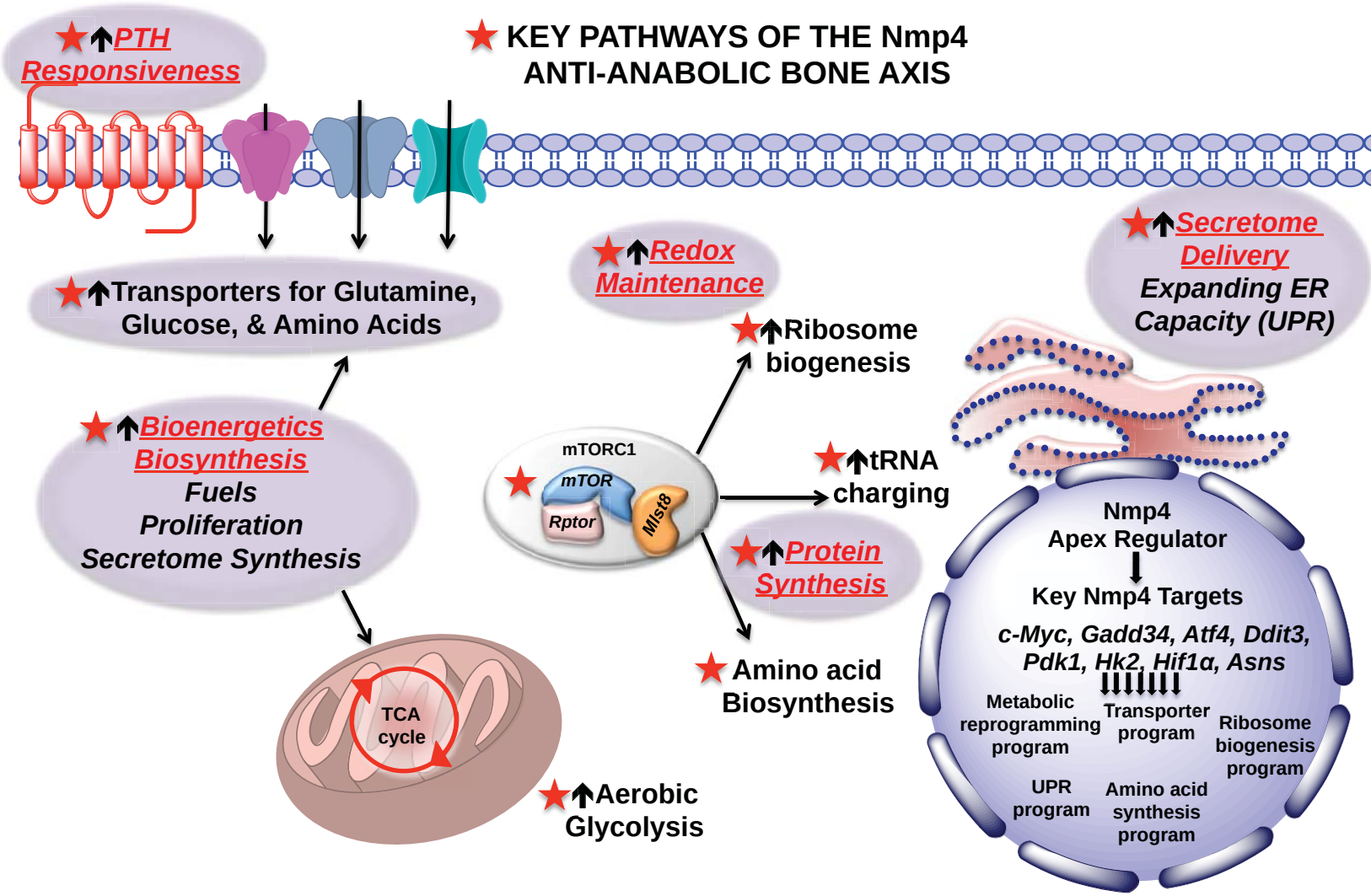
KEY PATHWAYS OF THE Nmp4
ANTI-ANABOLIC BONE AXIS
PTH Responsiveness
Transporters for Glutamine, Glucose, & Amino Acids
Redox Maintenance
Ribosome biogenesis
Secretome Delivery
Expanding ER Capacity (UPR)
Bioenergetics
Biosynthesis
Fuels
Proliferation
Secretome Synthesis
mTORC1
mTOR
Rptor
MIst8
tRNA charging
Protein Synthesis
Amino acid Biosynthesis
TCA cycle
Aerobic Glycolysis
Nmp4
Apex Regulator
Key Nmp4 Targets
c-Myc, Gadd34, Atf4, Ddit3, Pdk1, Hk2, Hif1α, Asns
Metabolic reprogramming program
Transporter program
Ribosome biogenesis program
UPR program
Amino acid synthesis program